

The inclusion of aerosols and clouds in
RTIASI, the ECMWF fast radiative
transfer model for the infrared
atmospheric sounding interferometer

Marco Matricardi

Research Department

July 2005

This paper has not been published and should be regarded as an Internal Report from ECMWF.
Permission to quote from it should be obtained from the ECMWF.



Series: ECMWF Technical Memoranda

A full list of ECMWF Publications can be found on our web site under:
<http://www.ecmwf.int/publications.html>

Contact: library@ecmwf.int

© Copyright 2005

European Centre for Medium Range Weather Forecasts
Shinfield Park, Reading, Berkshire RG2 9AX, England

Literary and scientific copyrights belong to ECMWF and are reserved in all countries. This publication is not to be reprinted or translated in whole or in part without the written permission of the Director. Appropriate non-commercial use will normally be granted under the condition that reference is made to ECMWF.

The information within this publication is given in good faith and considered to be true, but ECMWF accepts no liability for error, omission and for loss or damage arising from its use.

Abstract

A new version of RTIASI, the ECMWF fast radiative transfer model for the Infrared Atmospheric Sounding Interferometer (IASI) has been developed that features the introduction of multiple scattering by aerosols and clouds. In RTIASI, multiple scattering is parameterized by scaling the optical depth by a factor derived by including the backward scattering in the emission of a layer and in the transmission between levels (scaling approximation). The RTIASI radiative transfer can include by default eleven aerosol components, five types of water clouds and eight types of cirrus clouds. The database of optical properties for aerosols and water droplets has been generated using the Lorentz-Mie theory assuming these particles have a spherical shape. For cirrus clouds, a composite database of optical properties has been generated using the Geometric Optics method for large crystals and the T-matrix method for small crystals. In either case, ice crystals have been assumed to have the shape of a hexagonal prism randomly oriented in space. To solve the radiative transfer for an atmosphere partially covered by clouds, RTIASI uses a scheme (stream method) that divides the field of view into a number of homogeneous columns, each column containing either cloud-free layers or totally cloudy layers. Each column is assigned a fractional coverage and the number of columns is determined by the cloud overlapping assumption. The total radiance is then obtained as the sum of the radiances for the single columns weighted by the column fractional coverage. To assess the accuracy of the scaling approximation we have compared approximate radiances with reference radiances computed by using a doubling-adding algorithm. For aerosols, the largest errors are observed for the desert dust type. For this case, errors are less than 1 K in the thermal infrared and less than 0.25 K in the short wave. For water clouds, errors are typically less than 1K in the thermal infrared and less than 4 K in the short wave. For the cirrus cloud type, we found a remarkable agreement between approximate and reference radiances. For a tropical profile, errors introduced by the scaling approximation never exceed 0.5K whereas for an arctic profile errors are typically less than 0.1 K.

1. Introduction

Radiances from the Advanced TIROS Operational Vertical Sounder (ATOVS) on the National Oceanic and Atmospheric Administration (NOAA) polar orbiting satellites are used at the European Centre for Medium-Range Weather Forecasts (ECMWF) by assimilation the radiances directly into the four-dimensional variational analysis scheme, 4-DVAR (Rabier et. al. 1998). A potentially useful addition to the current satellite sounders is the Infrared Atmospheric Sounding Interferometer (IASI) (Cayla 1993). In combination with the Advanced Microwave Sounding Unit (AMSU-A), the Microwave Humidity Sounder (MHS), and the Advanced Very High Resolution Radiometer (AVHRR/3), IASI is the core payload of the European Organisation for Exploitation of Meteorological Satellites (EUMETSAT) Meteorological Operational Satellite (METOP-1) (Klaes et al. 2000) and will contribute to the primary mission objective of METOP-1 that is the measurement of meteorological parameters for NWP and climate models.

A prerequisite for exploiting radiances from conventional and high-resolution sounders is the availability of a fast radiative transfer model (usually called the observation operator) to predict a first guess radiance from the model fields (temperature, water vapour, ozone, surface emissivity and perhaps clouds in the future).

As part of the preparations being made at ECMWF to exploit the IASI datasets, RTIASI, the ECMWF fast radiative transfer model for IASI, has been developed (Matricardi and Saunders, 1999). The original version of RTIASI has undergone a number of significant upgrades (Matricardi 2003) that has led to the release of a number of different versions of the model. This paper deals with the methods that were applied to develop the most recent versions of RTIASI, RTIASI-5. In Section 2 we describe the radiative transfer used in RTIASI-5 to parameterize multiple scattering by aerosols and clouds. This has involved the generation of a database of optical properties for aerosols, water clouds and cirrus clouds discussed in Section 3, 4, and 5 respectively. In Section 6 we describe the method used to solve the radiative transfer in presence of an

atmosphere partially covered by clouds. Errors introduced by the parameterization for multiple scattering are discussed in Section 7 where approximate radiances are compared to radiances obtained by using a doubling-adding algorithm. Conclusions are given in Section 8.

2. The radiative transfer equation for multiple scattering

A pencil of radiation traversing a medium will in general have its energy attenuated by scattering and absorption. This attenuation is called extinction. For a nonscattering medium such as the one considered in RTIASI-4, absorption is the sole process of extinction whereas for a nonabsorbing medium scattering is the sole process of extinction. When radiation is scattered more than once, we have multiple scattering, an important process for atmospheres characterized by the presence of aerosols and clouds. The energy removed from the pencil of radiation is characterized by a quantity referred to as the extinction coefficient, β_e . The extinction coefficient is the sum of the absorption, β_a , and scattering, β_s , coefficients and the units are given in terms of length (cm^{-1}). When the extinction coefficient is divided by the particle number density, the quantity is referred to as the extinction cross section, σ_e . A useful quantity in radiative transfer is the single-scattering albedo, $\bar{\omega}$, defined as the ratio of the scattering coefficient to the extinction coefficient:

$$\bar{\omega} = \frac{\beta_s}{\beta_e} \quad (1)$$

The single-scattering albedo is often expressed in the form

$$1 - \bar{\omega} = \frac{\beta_a}{\beta_e} \quad (2)$$

If we consider a polarized electromagnetic wave, its polarization properties can be described by a set of four quantities called Stokes parameters, I , Q , U and V . The first and second parameters are referred to as the intensity (or radiance) and degree of polarization. The scattered electric vector can be expressed by

$$\begin{bmatrix} I \\ Q \\ U \\ V \end{bmatrix} = \frac{\sigma_s}{r^2 4\pi} \mathbf{P} \begin{bmatrix} I_o \\ Q_o \\ U_o \\ V_o \end{bmatrix} \quad (3)$$

In Eq. (3), the subscript o denotes the incident wave, r is the distance between the scattering particle and the point of observation, σ_s is the scattering cross section and \mathbf{P} is the scattering phase matrix that can be calculated from the electromagnetic theory and in general consists of 16 nonzero elements. Polarization can be a subject of interest for some applications. However, for the purpose of RTIASI-5 computations we shall only be considering the transformation of intensity to intensity

$$I = \frac{\sigma_s}{r^2 4\pi} P_{11} I_o \quad (4)$$

The angular distribution of the energy scattered by a particle is then described by the nondimensional parameter P_{11} , henceforth referred to as the phase function, P . For spherical particles or not spherical particles randomly oriented in space, the phase function can be expressed as a function of the scattering angle, Θ , the angle between the incident and scattering directions (see Figure 1).

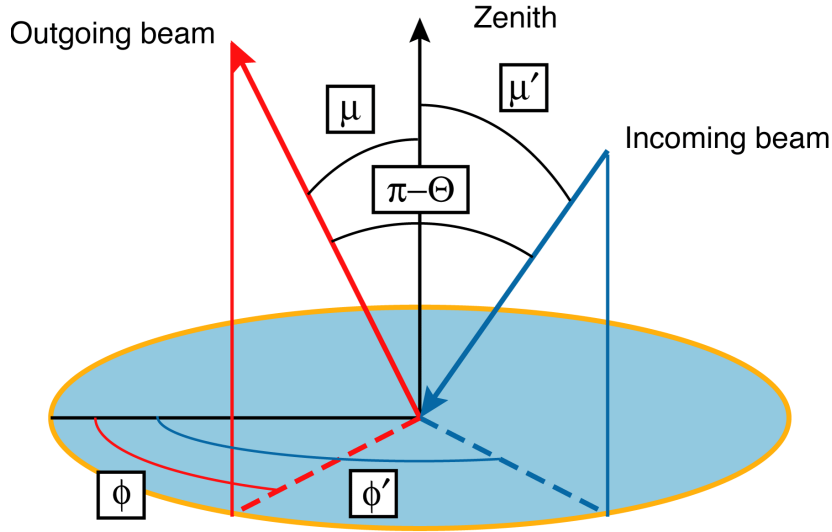


Figure 1. The relation between scattering, zenith and azimuthal angles.

We can relate the scattering angle to the incoming direction, (μ', ϕ') , and the outgoing direction, (μ, ϕ) , in the form

$$\cos(\Theta) = \mu\mu' + \sqrt{(1-\mu^2)}\sqrt{(1-\mu'^2)}\cos(\phi' - \phi) \quad (5)$$

where μ is the cosine of the zenith angle. The phase function is by definition normalized to unity

$$\frac{1}{4\pi} \int_0^{2\pi} \int_0^\pi P[\cos(\Theta)] \sin(\Theta) d\Theta d\phi = 1 \quad (6)$$

and we may define the azimuthally averaged phase function as

$$\bar{P}(\mu, \mu') = \frac{1}{2\pi} \int_0^{2\pi} P(\mu, \phi, \mu', \phi') d\phi' \quad (7)$$

An important parameter for radiative transfer is the asymmetry parameter, g , defined as the first moment of the phase function

$$g = \frac{1}{2} \int_{-1}^1 P(\cos(\Theta)) \cos(\Theta) d\cos(\Theta) \quad (8)$$

The asymmetry factor is positive if the phase function peaks in the forward direction and can be negative if the phase function peaks in the backward direction. In the limit of forward and backward scattering, g is equal to 1 and -1 respectively. Some approximated methods to solve the radiative transfer in presence of multiple scattering also require the computation of the second moment of the phase function, f ,

$$f = \frac{1}{2} \int_{-1}^1 P(\cos(\Theta)) \frac{1}{2} (3\cos^2(\Theta) - 1) d\cos(\Theta) \quad (9)$$

In RTIASI-5, the atmosphere is considered to be plane-parallel. In this stratified atmosphere we can assume that the atmospheric parameters and the radiance are functions of the vertical coordinate, z , alone (i.e. the distance measured along the direction of the local zenith taken to be perpendicular to the plane of stratification of the atmosphere). We can then define the normal optical depth as

$$\tau = \int_z^\infty \beta_e dz \quad (10)$$

and write the scalar radiative transfer equation for the diffuse azimuthally independent radiance, I , in the form

$$\mu \frac{dI(\tau, \mu)}{d\tau} = I(\tau, \mu) - \frac{\varpi}{2} \int_{-1}^1 I(\tau, \mu') \bar{P}(\mu, \mu') d\mu' - \frac{\varpi}{4\pi} F_\otimes \bar{P}(\mu, -\mu_\otimes) e^{\frac{-\tau}{\mu_\otimes}} - (1-\varpi)B[T(\tau)] \quad (11)$$

where $B[T(\tau)]$ is the Planck's function at temperature T , F_\otimes is the solar irradiance (flux density) at the top of the atmosphere and μ_\otimes is the solar zenith angle. The second term on the right hand side of Eq. (11) represents the multiple scattering of the diffuse radiance, the third term is the single scattering of the unscattered direct solar irradiance from the direction $(-\mu_\otimes, \phi_\otimes)$ and the fourth term is the atmospheric emission. Note that downward directions are denoted by negative μ 's. For the solar beam we adopt the convention to use a positive μ_\otimes so that $-\mu_\otimes$ is indicative of the fact that the solar beam is directed downward. For multiple scattering and absorption in presence of solar radiation we have to make the distinction between the diffuse radiance associated with multiple scattering and the directly transmitted solar radiance. Equation (11) describes the diffuse component. To account for the downward solar radiance we have to include the direct component that can be added separately using the Beer-Bouguer-Lambert law for extinction:

$$I_\otimes^\downarrow(\tau, \mu_\otimes) = \mu_\otimes F_\otimes e^{\frac{-\tau}{\mu_\otimes}} \quad (12)$$

For a detailed description how the surface reflection of the direct solar radiance is implemented in RTIASI, the user can refer to Matricardi (2003).

We can solve formally Eq. (11) for the upward, I^\uparrow , and downward, I^\downarrow , radiance for a homogeneous atmosphere bounded at $\tau = 0$ (top) and $\tau = \tau_1$ (bottom) in the form

$$I^\uparrow(0, \mu) = I^\uparrow(\tau_1, \mu) e^{\frac{-\tau_1}{\mu}} + \int_0^{\tau_1} J(\tau', \mu) e^{\frac{-\tau'}{\mu}} d\tau' / \mu \quad (13)$$

$$I^\downarrow(\tau, -\mu) = I^\downarrow(0, -\mu) e^{\frac{-\tau_1}{\mu}} + \int_0^{\tau_1} J(\tau', -\mu) e^{\frac{-(\tau-\tau')}{\mu}} d\tau' / \mu \quad (14)$$

where

$$J(\tau, \pm\mu) = \frac{\varpi}{2} \int_{-1}^1 I(\tau, \mu') \bar{P}(\pm\mu, \mu') d\mu' + \frac{\varpi}{4\pi} F_\otimes \bar{P}(\pm\mu, -\mu_\otimes) e^{\frac{-\tau}{\mu_\otimes}} + (1-\varpi)B[T(\tau)] \quad (15)$$

is the source function for scattering and emission. Since the source function includes the local radiation field, the solution to Eq. (11) is an integral equation. In principle numerical solutions to Eq. (11) (i.e. discrete ordinate and doubling adding method) are available that present few difficulties. However, within the framework of RTIASI-5 we can only consider an analytical solution given by approximate methods since

numerical solutions are too computationally expensive. A useful and accurate approximation is the two-stream approximation sometimes used in climate models (Liou 2002). The two-stream approximation can be obtained by replacing the integral in Eq. (11) by a summation using the Gauss quadrature and by expanding the azimuthally averaged phase function in terms of Legendre polynomials:

$$\begin{aligned} \mu_i \frac{dI(\tau, \mu_i)}{d\tau} &= I(\tau, \mu_i) - \frac{\varpi}{2} \sum_{l=0}^N \varpi_l P_l(\mu_i) \sum_{j=-n}^n I(\tau, \mu_j) P_l(\mu_j) a_j \\ &- \frac{\varpi}{4\pi} F_{\otimes} \left[\sum_{l=0}^N (-1)^l \varpi_l P_l(\mu_i) P_l(\mu_0) \right] e^{\frac{-\tau}{\mu_0}} - (1 - \varpi) B[T(\tau)] \end{aligned} \quad (16)$$

$$i = \pm 1, \dots, \pm n$$

where the quadrature point $\mu_{-j} = \mu_j, j \neq 0$, and the weight $a_{-j} = a_j$. The P_l 's are the Legendre polynomials. By setting $n=N=1$, the Gauss quadrature and weights are $\mu_1 = \frac{1}{\sqrt{3}}$ and $a_1 = 1$. Equation (16) then splits up into two first order differential equations

$$\frac{dI(\tau, \mu_1)}{d\tau} = \gamma_1 I(\tau, \mu_1) - \gamma_2 I(\tau, -\mu_1) - \gamma_3 B[T(\tau)] - \gamma_4 e^{\frac{-\tau}{\mu_0}} \quad (17)$$

$$\frac{dI(\tau, -\mu_1)}{d\tau} = \gamma_2 I(\tau, \mu_1) - \gamma_1 I(\tau, -\mu_1) + \gamma_3 B[T(\tau)] - \gamma_4^+ e^{\frac{-\tau}{\mu_0}} \quad (18)$$

where

$$\gamma_1 = \frac{(1 - \varpi(1 + g)/2)}{\mu_1} \quad (19)$$

$$\gamma_2 = \frac{\varpi(1 - g)}{2\mu_1} \quad (20)$$

$$\gamma_3 = \frac{(1 - \varpi)}{\mu_1} \quad (21)$$

$$\gamma_4^{\pm} = \frac{F_{\otimes} \varpi}{4\pi} (1 \pm 3g\mu_1\mu_0) \quad (22)$$

Solutions to Eqs. (16) and (17) can be derived in a straightforward way and are subjected to the radiation boundary conditions at the top and bottom of the layer. The upward, $I(\tau, \mu_1)$, and downward, $I(\tau, -\mu_1)$, radiances obtained from Eqs.(17) and (18) can be substituted in Eq. (15) to compute $J(\tau, \mu_1)$ and $J(\tau, -\mu_1)$ respectively. If we neglect the solar term, the source function $J(\tau, \mu_1)$ can then be written as

$$J(\tau, \mu_1) = Kve^{-k(\tau_1 - \tau)} + Hue^{-k\tau} + Z_1 e^{\frac{b\tau}{\tau_1}} \quad (23)$$

where

$$k = \sqrt{\gamma_1^2 - \gamma_2^2} \quad (24)$$

$$v = (1 - \mu_1 k) \quad (25)$$

$$u = a(1 + \mu_1 k) \quad (26)$$

$$Z_1 = B_0(1 - \varpi) \left(1 + \frac{\varpi(\gamma_1 + \gamma_2) + gb/\tau_1}{\mu_1(k^2 - b^2/\tau_1^2)} \right) \quad (27)$$

The upward radiance for a generic angle can then be obtained by substituting Eq.(23) into Eq.(13). An analytical solution is then possible and the form of the solution will depend on the way the Planck function B is parameterised. For illustrative purpose we parameterize the Planck function in the form

$$B(\tau) = B_0 e^{\frac{b\tau}{\tau_1}} \quad (28)$$

where τ_1 is the optical depth of the layer, B_0 is the Planck function at the top of the layer, B_1 is the Planck function at the bottom of the layer and $b = \ln\left(\frac{B_1}{B_0}\right)$. The upward radiance for an atmospheric layer bounded at the top and bottom by $\tau = 0$ and $\tau = \tau_1$ respectively, can then be written as

$$\begin{aligned} I^\uparrow(0, \mu) = & I(\tau_1, \mu) e^{-\frac{\tau_1}{\mu}} + \frac{Kv}{(1 - \mu k)} (e^{-k\tau_1} - e^{-\frac{\tau_1}{\mu}}) + \frac{Hu}{(1 + k\mu)} (1 - e^{-\tau_1(k+1/\mu)}) \\ & + \frac{Z_1}{(1 - b\mu/\tau_1)} (B_0 - B_1 e^{-\tau_1/\mu}) \end{aligned} \quad (29)$$

The constants K and H are determined from the boundary conditions at the top and bottom of the layer and are functions of the layer optical depth. To obtain the radiance for an IASI channel, the monochromatic radiance $I^\uparrow(0, \mu)$ has to be convolved with the IASI spectral response function. Since RTIASI uses the polychromatic form of the radiative transfer equation, the convolution of $I^\uparrow(0, \mu)$ is replaced by the radiance obtained by using convolved quantities in Eq. (29). Since $I^\uparrow(0, \mu)$ is a complex function of optical depth, it is not obvious the use of the polychromatic approximation would be accurate enough to be incorporated in RTIASI-5. To test the accuracy of the polychromatic approximation for the two-stream model we have computed monochromatic radiances at the IASI ‘‘infinite resolution’’ of 0.001 cm^{-1} and compared the convolved radiances with the polychromatic ones. Trials were carried out for a tropical and arctic profile including a low-level water cloud, a cirrus cloud and an optically thick aerosol type. Results show that the two-stream approximation is not amenable to incorporation in RTIASI since this result in errors that are order of magnitudes larger than the instrument noise and what matters most, larger than the errors introduced by the multiple scattering parameterisation introduced in RTIASI-5 (see below for details). It should also be stressed that the computational burden of the two-stream approximation can become very significant is a large number of channels is to be processed.

On this basis we have looked into an alternative treatment of multiple scattering in RTIASI-5 that would allow us to retain some degree of accuracy without compromising the computational efficiency of the code. The scheme we have introduced is based on the approach followed by Chou et al. (1999). In this scheme (henceforth referred to as scaling approximation), the effect of scattering by clouds and aerosols is parameterised by scaling the optical depth by a factor derived by including the backward scattering in the emission of a layer and in the transmission between levels. Since this parameterisation of multiple scattering rests of the hypothesis that the diffuse radiance field is isotropic and can be approximated by the Planck

function, we can expect it to have an effect on the accuracy of the radiance calculations. However, the scaling approximation has the advantage that the form of the radiative transfer equation does not differ too much from the one used in clear sky conditions and thus the computational efficiency of the code is not significantly degraded.

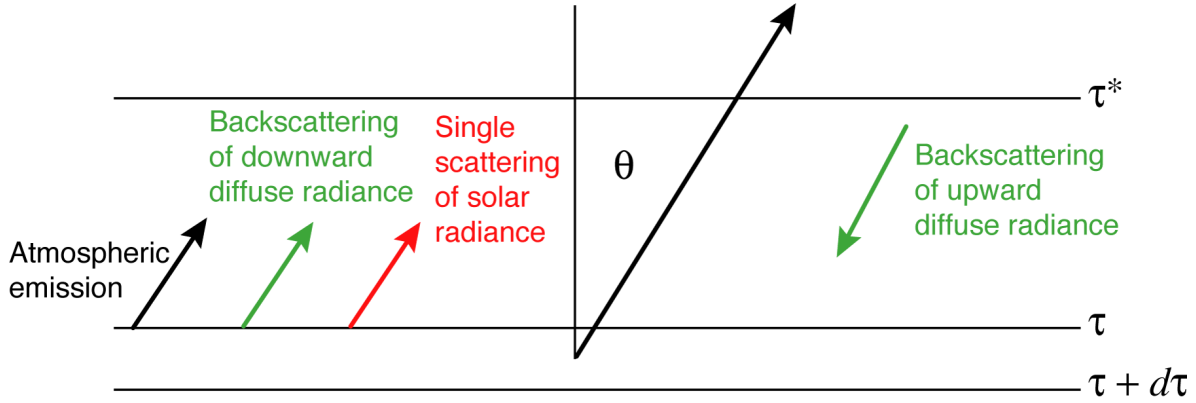


Figure 2 Schematic contribution of the layer $d\mathcal{G}$ to the upward radiance at \mathcal{G}' .

To derive the scaling approximation we can refer to Figure 2 and note that a homogeneous atmospheric layer of thickness dz bounded by $\tau + d\tau$ and τ will emit and reflect radiation in the direction μ . To evaluate the contribution of the layer dz to the upward radiation at τ^* , we have to consider the absorption and scattering of radiation between τ and τ^* . We can define the apparent emission, $dI'(\tau, \mu)$, of the layer $d\tau$ in the direction μ as the sum of the radiance emitted and reflected by the layer in the direction μ :

$$dI'(\tau, \mu) = \frac{d\tau}{\mu} \frac{\varpi}{2} \int_{-1}^0 I(\tau, \mu') \bar{P}(\mu, \mu') d\mu' + (1 - \varpi) B[T(\tau)] d\tau / \mu \quad (30)$$

If we assume that the diffuse radiance field, $I(\tau, \mu')$, is isotropic and it can be approximated by $B[T(\tau)]$, we can then write the apparent emission as

$$dI'(\tau, \mu) = [1 - \varpi (1 - b)] B[T(\tau)] d\tau / \mu \quad (31)$$

where

$$b = \frac{1}{2} \int_0^1 d\mu \int_{-1}^0 \bar{P}(\mu, \mu') d\mu' \quad (32)$$

is the integrated fraction of energy scattered backward for incident radiation from above or below. To compute the upward radiance at τ^* we need to know the transmittance between τ and τ' . If we associate the optical depth with either the radiation absorbed and backward scattered, we can approximate the apparent optical depth for extinction, $d\tilde{\tau}$, for a layer $d\tau$ as

$$d\tilde{\tau} = d\tau_a + b d\tau_s = [1 - \varpi(1 - b)] d\tau \quad (33)$$

where $\varpi = \frac{d\tau_s}{d\tau}$. Based on Eqs. (30), (31), (32) and (33) the upward radiance for a homogeneous atmosphere bounded at $\tau = 0$ (top) and $\tau = \tau_1$ (bottom) can now be written as

$$I^\uparrow(0, \mu) = I^\uparrow(\tilde{\tau}_1, \mu) e^{-\frac{\tilde{\tau}_1}{\mu}} + \int_0^{\tilde{\tau}_1} B[T(\tilde{\tau})] e^{-\frac{\tilde{\tau}'}{\mu}} d\tilde{\tau}' / \mu + \frac{\varpi F_\otimes \bar{P}(\mu, -\mu_0)}{4\pi\mu} \int_0^{\tilde{\tau}_1} e^{-\tilde{\tau}'(\frac{1}{\mu} + \frac{1}{\mu_\otimes})} d\tilde{\tau}' \quad (34)$$

where

$$\tilde{\tau} = \tau_a + b\tau_s \quad (35)$$

$$\varpi = \frac{\tau_s}{\tau_a + \tau_s} \quad (36)$$

and the third term on the left-hand side of Eq.(34) is the contribution from the single scattering of the solar beam. Similar considerations can be applied to obtain the downward radiance.

As noted previously, the final form of Eq. (34) will depend on the way the Planck function, B , is parameterised. In the previous version of RTIASI it was assumed that the atmospheric layer can be considered to be sufficiently optically thin that equal weight can be given to radiance emitted from all regions within the layer, i.e. the value of the Planck function evaluated at the average temperature of the layer is used. In presence of optically thick clouds one expects only the upper regions of the layer to give a significant contribute to the radiance. In this case the use of the average value of the Planck function would put too much weight on the radiance coming from the lower regions of the layer. To improve the accuracy of radiance calculations in RTIASI-5, we have introduced a new parameterisation of the Planck function based on the linear in τ assumption that the source function throughout the layer is linear with the optical depth of the layer:

$$B[T(\tau)] = B_0 + (B_1 - B_0) \frac{\tilde{\tau}}{\tilde{\tau}^*} \quad (37)$$

where B_u is the Planck function for the top of the layer, B_b is the Planck function at the bottom of the layer and $\tilde{\tau}^*$ is the optical depth of the layer. The parameterisation is exact at the top ($\tilde{\tau} = 0$) and bottom ($\tau = \tilde{\tau}^*$) of the layer. The new formulation of the layer source function has been applied to RTIASI-5 and top of the atmosphere brightness temperatures, B_τ , have been compared with the ones, B_m , resulting from the application of the mean layer source function used in RTIASI-4. Results are shown in Figures 3 and 4 where the difference $B_m - B_\tau$ is plotted for two atmospheric profiles (#1 and #36) selected from the dataset of 117 independent profiles used to test the accuracy of the fast transmittance model. In clear sky conditions the application of the new source function results in differences across the spectrum up to 0.15 K and, with the exception of the 4.2 μ m band, smaller values are found for the arctic profile. For both profiles the sign of the departures changes for the stratospheric channels (the temperature of the bottom of the layer is greater than the temperature of the top of the layer) and larger errors are found for the bands with larger optical depths.

When a low cloud with cloud top height of 2 km is introduced in a 320-m-thick layer, a different behaviour is observed with departures significantly larger than the ones for the clear sky case. As shown in Figure 4, the application of the new source function now results in differences across the spectrum up to 0.7 K with smaller values found for the arctic profile. As expected, the presence of the cloud does not affect the spectrum for the stratospheric channels and larger differences are found in the bands with smaller optical depths. For these bands the change of the sign of the departures for the arctic profile is the result of a temperature inversion in the layer where the cloud was placed. Results shown in Figure 4 can serve as a guide to the improved accuracy that can be achieved by introducing the linear in τ source function in the

radiative transfer in presence of clouds. As shown in Amorati and Rizzi (2002), the error introduced by the mean layer source function increases with the optical depth of the cloud and tends to an asymptotic value for large optical depths. Given the vertical pressure grid used in RTIASI-5, we expect this error not to exceed 2 K.

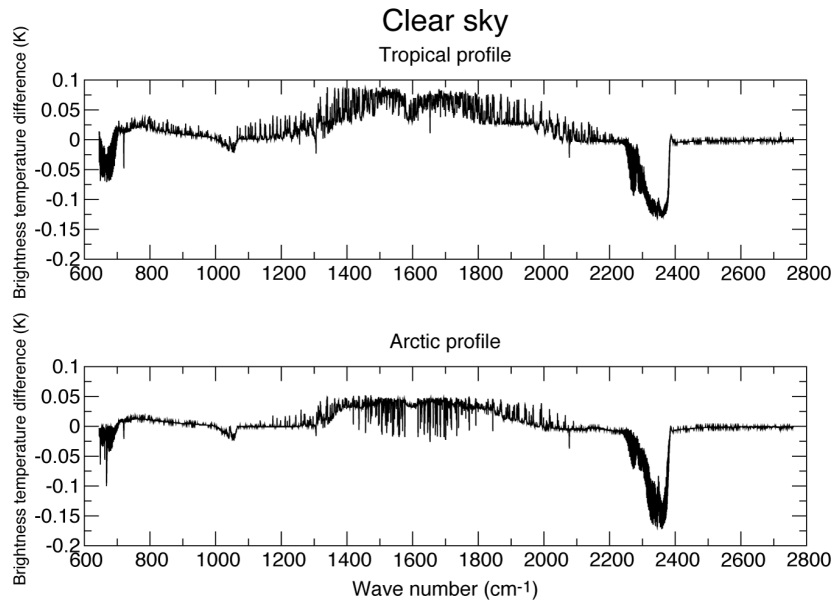


Figure 3 Differences in the top of the atmosphere brightness temperatures calculated using RTIASI with the mean layer and linear in τ source function definitions.

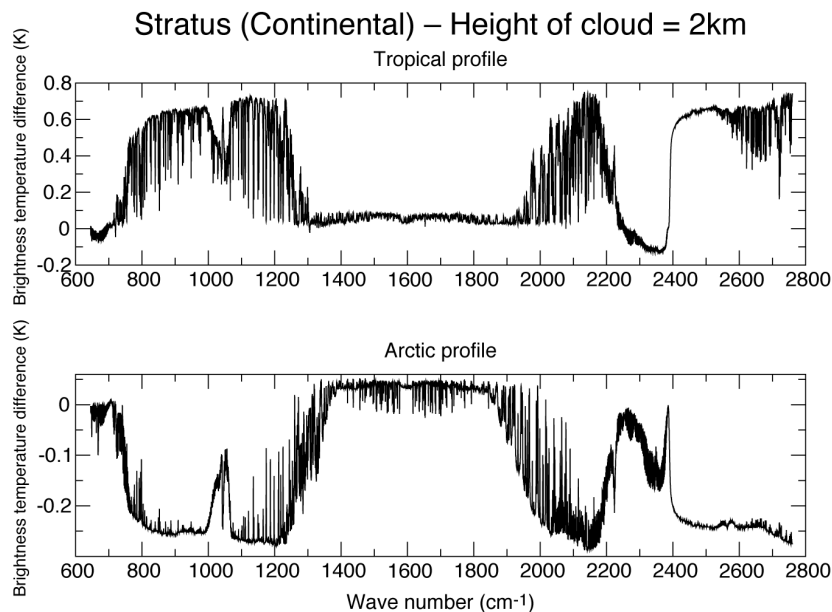


Figure 4 Differences in the top of the atmosphere brightness temperatures calculated using RTIASI with the mean layer and linear in τ source function definitions.

Using the ‘linear in τ ’ assumption for the phase function we can now write the upward and downward radiance for a homogeneous atmosphere bounded at $\tau = 0$ (top) and $\tilde{\tau}$ (bottom) in the form

$$\begin{aligned}
 I^\uparrow(0, \mu) &= I^\uparrow(\tau, \mu)e^{-\frac{\tau}{\mu}} + B_0(1 - e^{-\frac{\tau}{\mu}}) - (B_1 - B_0)e^{-\frac{\tau}{\mu}} + \frac{(B_1 - B_0)\mu}{\tilde{\tau}}(1 - e^{-\frac{\tau}{\mu}}) \\
 &+ \frac{\mu_\otimes \varpi F_\otimes \bar{P}(\mu, -\mu_\otimes)}{4\pi(\mu + \mu_\otimes)}(1 - e^{-\frac{\tau}{\mu}(\frac{1}{\mu} + \frac{1}{\mu_\otimes})})
 \end{aligned} \tag{38}$$

$$\begin{aligned}
 I^\downarrow(\tau, -\mu) &= I^\downarrow(0, -\mu)e^{-\frac{\tau}{\mu}} + B_0(1 - e^{-\frac{\tau}{\mu}}) + (B_1 - B_0) - \frac{(B_1 - B_0)\mu}{\tilde{\tau}}(1 - e^{-\frac{\tau}{\mu}}) \\
 &+ \frac{\mu_\otimes \varpi F_\otimes \bar{P}(-\mu, -\mu_\otimes)}{4\pi(\mu - \mu_\otimes)}(e^{-\frac{\tau}{\mu}} - e^{-\frac{\tau}{\mu_\otimes}})
 \end{aligned} \quad \mu \neq \mu_\otimes \tag{39}$$

$$\begin{aligned}
 I^\downarrow(\tau, -\mu) &= I^\downarrow(0, -\mu)e^{-\frac{\tau}{\mu}} + B_0(1 - e^{-\frac{\tau}{\mu}}) + (B_1 - B_0) - \frac{(B_1 - B_0)\mu}{\tilde{\tau}}(1 - e^{-\frac{\tau}{\mu}}) \\
 &+ \frac{\tilde{\tau} \varpi F_\otimes \bar{P}(-\mu, -\mu_\otimes)}{4\pi\mu_\otimes}(e^{-\frac{\tau}{\mu_\otimes}})
 \end{aligned} \quad \mu = \mu_\otimes \tag{40}$$

Equations (38), (39) and (40) can be extended to a vertically non-homogeneous atmosphere by dividing the atmosphere into a number of homogeneous layers. If there is no downward diffuse radiance at the top of the atmosphere (i.e. $I^\downarrow(0, -\mu) = 0$) and assume specular reflection at the Earth's surface, then by applying the condition that the upward and downward diffuse radiances must be continuous at the interface of each layer, we can write Eqs. (38), (39) and (40) in discrete layer notation in the form

$$\begin{aligned}
 I^\uparrow &= B(T_s)\Gamma_s \varepsilon_s + I^\downarrow(1 - \varepsilon_s)\Gamma_s + \sum_{j=1}^N \{B_0(\Gamma_j - \Gamma_{j+1}) - B_1\Gamma_{j+1} + B_1 \frac{\mu}{\tau_j}(\Gamma_j - \Gamma_{j+1}) + \\
 &F_\otimes \varpi \mu_\otimes \frac{\bar{P}(\mu, -\mu_\otimes)}{4\pi(\mu + \mu_\otimes)}(\Gamma_j - \Gamma_{j+1}e^{-\frac{\tau_j}{\mu_\otimes}})\}
 \end{aligned} \tag{41}$$

$$\begin{aligned}
 I^\downarrow &= \sum_{j=1}^N \{B_0 \frac{(\Gamma_j - \Gamma_{j+1})\Gamma_s}{\Gamma_j \Gamma_{j+1}} + B_1 \frac{\Gamma_j \Gamma_s}{\Gamma_{j+1}^2} - B_1 \frac{\mu}{\tau_j} \frac{(\Gamma_j - \Gamma_{j+1})\Gamma_s}{\Gamma_j \Gamma_{j+1}} + \\
 &F_\otimes \varpi \mu_\otimes \frac{\bar{P}(-\mu, -\mu_\otimes)}{4\pi(\mu - \mu_\otimes)} \frac{(\Gamma_{j+1} - \Gamma_j e^{-\frac{\tau_j}{\mu_\otimes}})\Gamma_s}{\Gamma_{j+1} \Gamma_j}\}
 \end{aligned} \quad \mu \neq \mu_\otimes \tag{42}$$

$$\begin{aligned}
 I^\downarrow &= \sum_{j=1}^N \{B_0 \frac{(\Gamma_j - \Gamma_{j+1})\Gamma_s}{\Gamma_j \Gamma_{j+1}} + B_1 \frac{\Gamma_j \Gamma_s}{\Gamma_{j+1}^2} - B_1 \frac{\mu}{\tau_j} \frac{(\Gamma_j - \Gamma_{j+1})\Gamma_s}{\Gamma_j \Gamma_{j+1}} + \\
 &F_\otimes \varpi \frac{\bar{P}(-\mu, -\mu_\otimes)}{4\pi\mu_\otimes} \frac{e^{-\frac{\tau_j}{\mu_\otimes}} \Gamma_s \tilde{\tau}_j}{\Gamma_{j+1}}\}
 \end{aligned} \quad \mu = \mu_\otimes \tag{43}$$

where Γ_j is the transmittance from level j to the top of the atmosphere, Γ_s is the transmittance from the surface to the top of the atmosphere, $\tilde{\tau}_j$ is the normal optical depth for layer j , N is the number of layers the atmosphere is divided into, T_s is the surface temperature and ε_s is the hemispherical emissivity of the surface. Note that we take $\Gamma_1 = 1$.

When implementing Eqs. (41), (42) and (43) we have to consider the occurrence of negative transmittances in RTIASI-5. This is the result of a process where transmittances are reset to small negative values when a threshold value is reached. This operation is performed to make fast model transmittances to be consistent with line-by-line equivalents. For the layer where the switch to the negative transmittances occur, the layer optical depth $\tilde{\tau}_j$ cannot be defined and this renders the implementation of the linear in τ source function not applicable to this layer. In clear sky conditions this layer makes a negligible contribution to the top of the atmosphere radiance and we can replace the linear in τ source function with the mean layer source function that does not require the computation of the layer optical depth. However, if the switch to the negative transmittance is triggered by the presence of aerosols or clouds in the layer, to reconcile fast model radiances with line-by-line equivalents the value of the linear in τ source function is computed by using the top of the layer positive and bottom of the layer negative transmittance and the actual value of the layer optical depth, $\tilde{\tau}_j$, (i.e. the sum of the molecular and aerosol/cloud optical depth) even though this value is not physically related to the negative value of the transmittance at the bottom of the layer.

3. The dataset of optical properties for aerosols

The interaction of a plane wave with a dielectric sphere can be solved exactly by the Lorentz-Mie theory of light scattering by spheres (Van de Hulst 1981). The geometry of aerosol particles can vary from quasi-spherical to highly irregular. The size of an aerosol particle is typically of the order of $0.1\mu\text{m}$ but particles as large as 10 to $20\mu\text{m}$ have been observed. In this paper aerosols are assumed to have a spherical shape. The optical properties for the aerosols included in RTIASI-5 are computed using the dataset of microphysical properties assembled in the Optical Properties of Aerosols and Clouds (OPAC) software package (Hess et al. 1998). This dataset provides the microphysical properties for ten aerosol components. The aerosol components reflect the range of sources and processes found at any place in the atmosphere.

If we consider a sample aerosol particles and describe their size spectrum by $n(r)$ (in units of $\text{cm}^{-3} \mu\text{m}^{-1}$), if the size of particles ranges from r_{\min} to r_{\max} the total number density of particles is given by

$$N = \int_{r_{\min}}^{r_{\max}} n(r) dr \quad (44)$$

For each of the aerosol component considered in OPAC a lognormal size distribution is used

$$n_i(r) = \frac{N_i}{\sqrt{2\pi r \log(\sigma_i) \ln(10)}} \exp \left[-\frac{1}{2} \left(\frac{\log(r) - \log(r_{\text{mod},i})}{\log(\sigma_i)} \right)^2 \right] \quad (45)$$

where $r_{\text{mod},i}$ is the mode radius, σ_i is the width of the distribution and N_i is the total number density in units of cm^{-3} . In RTIASI-5 we follow the convention adopted in OPAC to normalize the size distribution to a number density of $1 \text{ particle cm}^{-3} \mu\text{m}^{-1}$ (henceforth referred to as $n_i^1(r)$). For a sample of aerosol particles the

scattering coefficient, extinction coefficient, phase function and asymmetry parameter is then defined as follows:

$$\beta_{e,i} = N_i \beta_{e,i}^1 = N_i \int_{r_{\min}}^{r_{\max}} \sigma_{e,i}(r) n_i^1(r) dr \quad (46)$$

$$\beta_{s,i} = N_i \beta_{s,i}^1 = N_i \int_{r_{\min}}^{r_{\max}} \sigma_{s,i}(r) n_i^1(r) dr \quad (47)$$

$$P_i(\Theta) = \frac{\int_{r_{\min}}^{r_{\max}} P_i(\Theta, r) \sigma_{s,i}(r) n_i^1(r) dr}{\int_{r_{\min}}^{r_{\max}} \sigma_{s,i}(r) n_i^1(r) dr} \quad (48)$$

$$g_i = \frac{\int_{r_{\min}}^{r_{\max}} g_i(r) \sigma_{s,i}(r) n_i^1(r) dr}{\int_{r_{\min}}^{r_{\max}} \sigma_{s,i}(r) n_i^1(r) dr} \quad (49)$$

Relative humidity affects the shape as well as the size of aerosols. For those aerosols that interact with water vapour, microphysical properties are given for eight different values of the relative humidity assuming the width of the distribution does not change. In RTIASI-5, for an arbitrary water vapour and temperature profile, the microphysical properties for these aerosols are obtained by linear interpolation to the actual value of the relative humidity. We have tabulated the microphysical properties of the OPAC aerosol components in Table 1 and plotted the aerosol components size distribution (normalized to 1 particle cm^{-3}) in Figures 5 and 6 (for a 0 % value of the relative humidity).

Component	R_{mod} ($\mu\text{ m}$)	R_{min} ($\mu\text{ m}$)	R_{max} ($\mu\text{ m}$)	σ	Relative humidity (%)
Insoluble	0.471	0.005	20	2.51	Not affected
Water-soluble	0.0212	0.005	20	2.24	0
Water-soluble	0.0262	0.006	25	2.24	50
Water-soluble	0.0285	0.0064	27.4	2.24	70
Water-soluble	0.0306	0.0067	29.8	2.24	80
Water-soluble	0.0348	0.0071	35	2.24	90
Water-soluble	0.0399	0.0074	42.8	2.24	95
Water-soluble	0.0476	0.0078	58.5	2.24	98
Water-soluble	0.0534	0.0079	74.9	2.24	99
Soot	0.0118	0.005	20	2.00	Not affected
Sea salt (acc.mode)	0.209	0.005	20	2.03	0
Sea salt (acc.mode)	0.336	0.0077	32.2	2.03	50
Sea salt (acc.mode)	0.378	0.0085	36.3	2.03	70
Sea salt (acc.mode)	0.416	0.0090	39.9	2.03	80
Sea salt (acc.mode)	0.497	0.0099	47.8	2.03	90
Sea salt (acc.mode)	0.605	0.0108	58.5	2.03	95
Sea salt (acc.mode)	0.801	0.0115	78.3	2.03	98
Sea salt (acc.mode)	0.995	0.0118	98.5	2.03	99
Sea salt (coa.mode)	1.75	0.005	60	2.03	0
Sea salt (coa.mode)	2.82	0.0077	90.5	2.03	50
Sea salt (coa.mode)	3.17	0.0085	100	2.03	70
Sea salt (coa.mode)	3.49	0.0090	100	2.03	80
Sea salt (coa.mode)	4.18	0.0099	100	2.03	90
Sea salt (coa.mode)	5.11	0.0108	100	2.03	95
Sea salt (coa.mode)	6.84	0.0115	100	2.03	98
Sea salt (coa.mode)	8.59	0.0118	100	2.03	99
Mineral(nuc. mode)	0.07	0.005	20	1.95	Not affected
Mineral(acc.mode)	0.39	0.005	20	2	Not affected
Mineral(coa.mode)	1.9	0.005	60	2.15	Not affected
Mineral-transported	0.5	0.02	5	2.20	Not affected
Sulphate droplets	0.0695	0.005	20	2.03	0
Sulphate droplets	0.0983	0.0073	30.2	2.03	50
Sulphate droplets	0.109	0.0079	33.6	2.03	70
Sulphate droplets	0.118	0.0084	36.4	2.03	80
Sulphate droplets	0.135	0.0090	42.3	2.03	90
Sulphate droplets	0.158	0.0096	50.2	2.03	95
Sulphate droplets	0.195	0.101	65.5	2.03	98
Sulphate droplets	0.231	0.0103	81.8	2.03	99

Table 1. The microphysical properties of the OPAC aerosols components

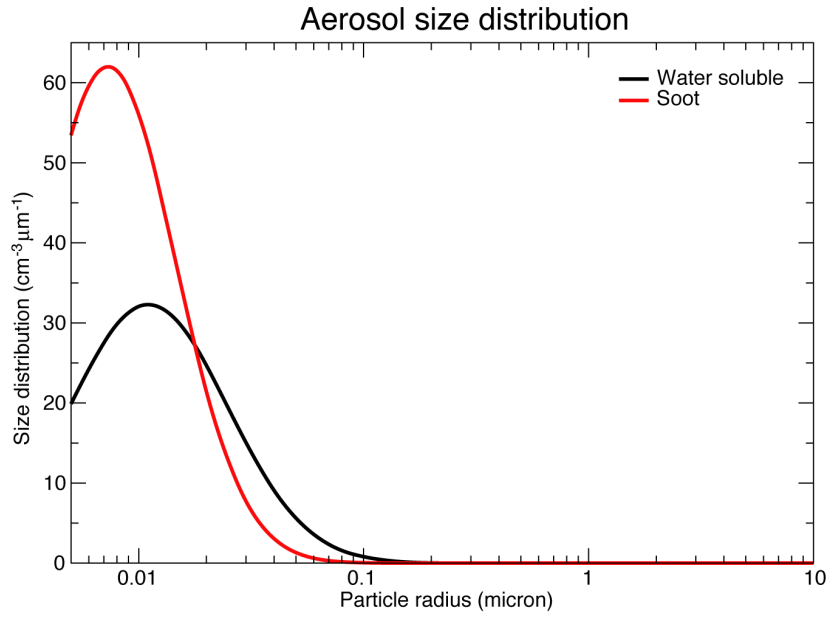


Figure 5. The normalized size distribution for the aerosol components defined in RTIASI-5.

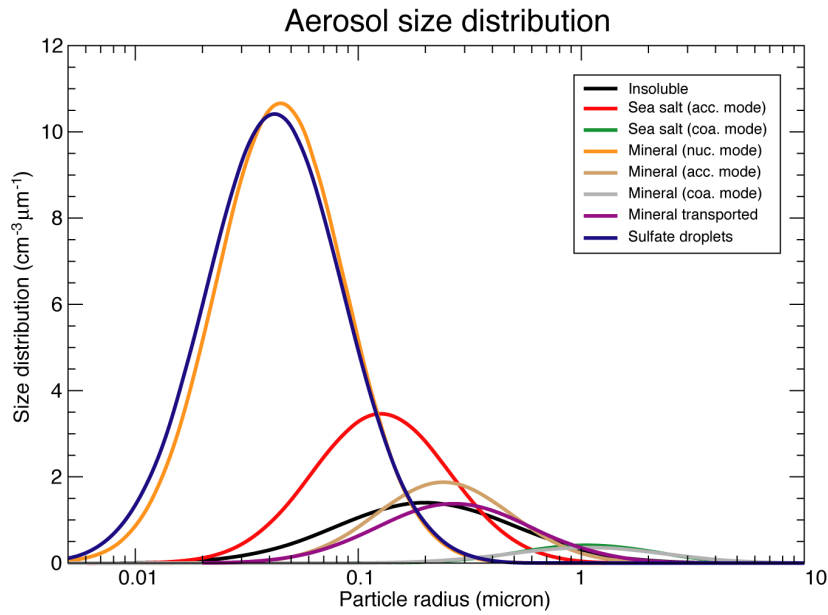


Figure 6 The normalized size distribution for the aerosol components defined in RTIASI-5.

To be able to simulate the radiative properties of the atmosphere in presence of a volcanic eruption, we have supplemented the OPAC aerosol components with the volcanic ash component. For this component a modified Gamma size distribution is assumed

$$n(r) = N_i a r^\alpha \exp\left[-\frac{\alpha}{\gamma} \left(\frac{r}{r_{mod,i}}\right)^\gamma\right] \tag{50}$$

where α and γ describe the slope of the distribution and a is a normalizations factor. The microphysical properties for volcanic ash are listed in Table 2 (Trotsenko 2003).

Component	R_{mod} (μm)	R_{min} (μm)	R_{max} (μm)	α	γ	a
Volcanic ash	0.0156	0.005	20	1	0.5	5461

Table 2. The microphysical properties of volcanic ash aerosol component

The database of aerosols optical properties used in RTIASI-5 has been generated using the Lorentz-Mie theory. The real and imaginary components of the aerosols refractive index are taken from the OPAC package. For the IASI spectral range, refractive indices are given at 31 different frequencies. These refractive indices have been interpolated to the central wavelength of each of the 8461 IASI channels and then used to compute the absorption coefficient, scattering coefficient, extinction coefficient, phase function, asymmetry parameter, second moment of the phase function and the b parameter defined in Eq. (32) for every single aerosol component. Values of the phase function are given for every 0.1° from 0° to 3° otherwise they are given for every 1° . This makes a total of 208 scattering angles. Note that although in principle the computation of the b parameter presents no difficulties, this requires the azimuthal averaging of the phase function for each combination of the 208 discrete scattering angles. Hence, an accurate computation of the b parameter for each of the 8461 IASI channels requires a significant amount of computational time. Finally, it should be stressed that since the refractive indices are a slowly varying function of the wavelength, we can consider the optical properties of aerosols to be constant over the width of an IASI channel.

Aerosols can be classified in terms of their location (i.e. continental, maritime, polar) and type (i.e. clear, polluted, desert, urban). For each type/location a number of aerosol components is involved. In principle a wide range of possible compositions is possible. For a mixture of M aerosol components the resulting optical properties are defined as follows:

$$\beta_e = \sum_{i=1}^M N_i \beta_{e,i}^1 \quad (51)$$

$$\beta_s = \sum_{i=1}^M N_i \beta_{s,i}^1 \quad (52)$$

$$P(\Theta) = \frac{\sum_{i=1}^M P_i(\Theta) N_i \beta_{s,i}^1}{\beta_s} \quad (53)$$

$$g = \frac{\sum_{i=1}^M g_i N_i \beta_{s,i}^1}{\beta_s} \quad (54)$$

$$b = \frac{\sum_{i=1}^M b_i N_i \beta_{s,i}^1}{\beta_s} \quad (55)$$

In every atmospheric layer the RTIASI-5 user can define any mixture of aerosol components and then obtain the optical properties for a given situation by specifying the number densities of the single aerosol components. However, the user should be aware of the fact that for the number densities to be meaningful, they should be assigned in such a way as to reflect the relative magnitude of the size distribution. With reference to Figures 5 and 6, larger number densities should be assigned to components characterized by larger values of the size distribution.

For those users that are interested in sensitivity studies, RTIASI-5 can compute the optical properties for 10 aerosol types representative of average and extreme conditions for what is considered to be the range of climatological important aerosols. The composition of the aerosol types included in RTIASI-5 is tabulated in Table 3. In Figures 7 and 8 we have plotted the optical properties for the five most significant (in radiative terms) aerosol types. For all aerosol types plotted in Figures 7 and 8, the single scattering albedo in the shortwave is larger than the single scattering albedo in the longwave and so it is the asymmetry parameter. Also note the relative magnitude of the absorption, scattering and extinction coefficient and how the optical thickness of the desert aerosol is by far the largest among the ones considered in this paper.

Aerosol type	Component	N_i (cm^{-3})
Continental clean	Water soluble	2600
	Insoluble	0.15
Continental average	Water soluble	7000
	Insoluble	0.4
	Soot	8300
Continental polluted	Water soluble	15700
	Insoluble	0.6
	Soot	34300
Urban	Water soluble	28000
	Insoluble	1.5
	Soot	130000
Desert	Water soluble	2000
	Mineral (nucl.)	296.5
	Mineral (acc.)	30.5
	Mineral (coa.)	0.142
Maritime clean	Water soluble	1520
	Sea salt (acc.)	20
	Sea salt (coa.)	3.2E-03
Maritime polluted	Water soluble	9000
	Sea salt (acc.)	20
	Sea salt (coa.)	3.2E-03
	Soot	5180
Maritime tropical	Water soluble	590
	Sea salt (acc.)	10
	Sea salt (coa.)	1.3E-03
Arctic	Water soluble	1300
	Insoluble	0.001
	Sea salt (acc.)	1.9
	Soot	5300
Antarctic	Sulphate droplets	42.9
	Sea salt (acc.)	0.47E-01
	Mineral transported	0.53E-02

Table 3. Composition of aerosol types included in RTIASI-5.

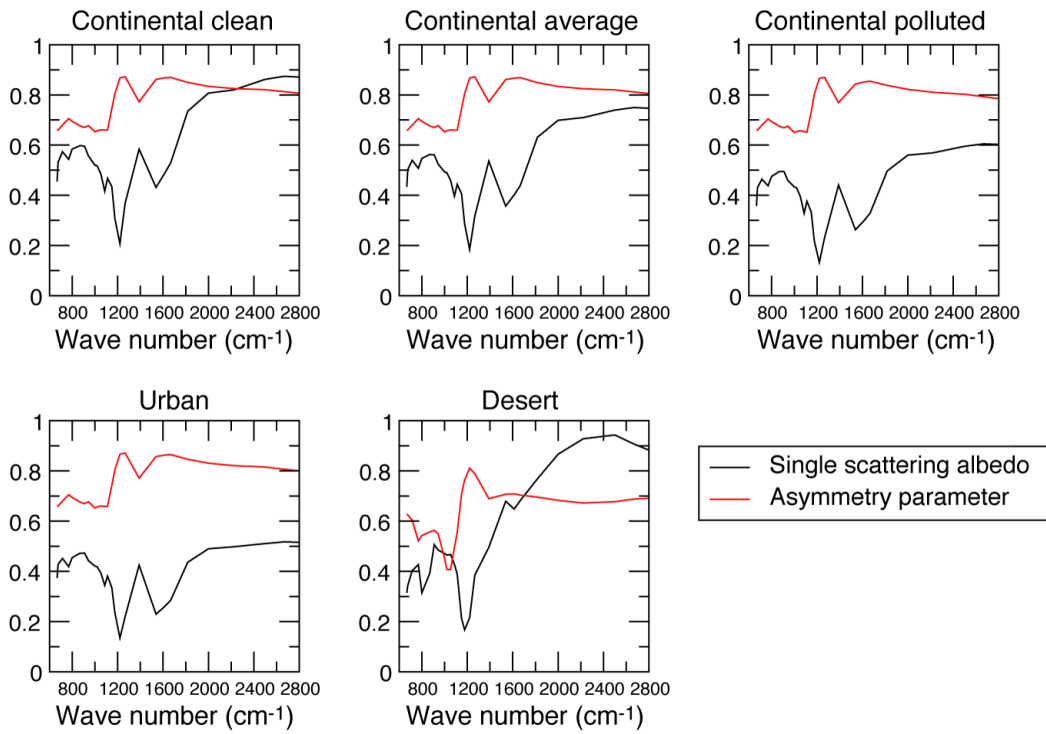


Figure 7 The single scattering albedo and asymmetry parameter for five of the aerosol types included in RTIASI-5.

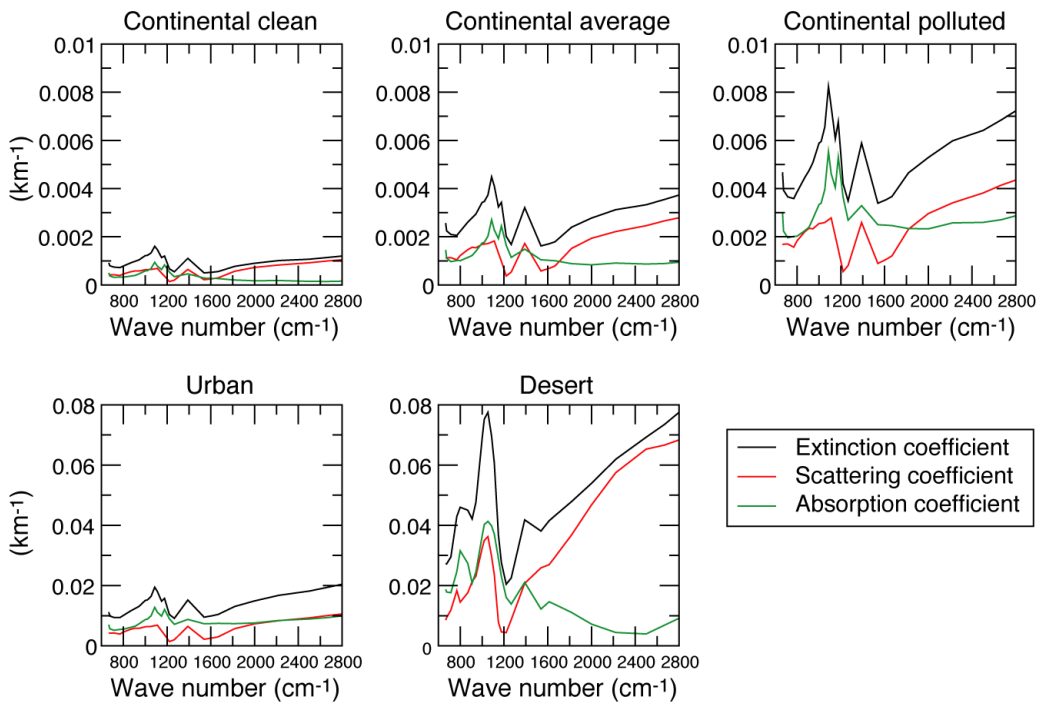


Figure 8 The absorption, scattering and extinction coefficient for five of the aerosol types included in RTIASI-5.

4. The dataset of optical properties for water clouds

Water clouds are by their nature composed of spherical water droplets whose size ranges from ~1 μm to 20 μm. The OPAC package gives the microphysical properties for 5 types of water clouds: two stratus clouds and 3 cumulus clouds. The size distribution for these clouds is described by the modified Gamma distribution (see Eq. (50)). The size distribution normalized to 1 particle cm⁻³ is plotted in Figure 9 for all the cloud types considered in this paper.

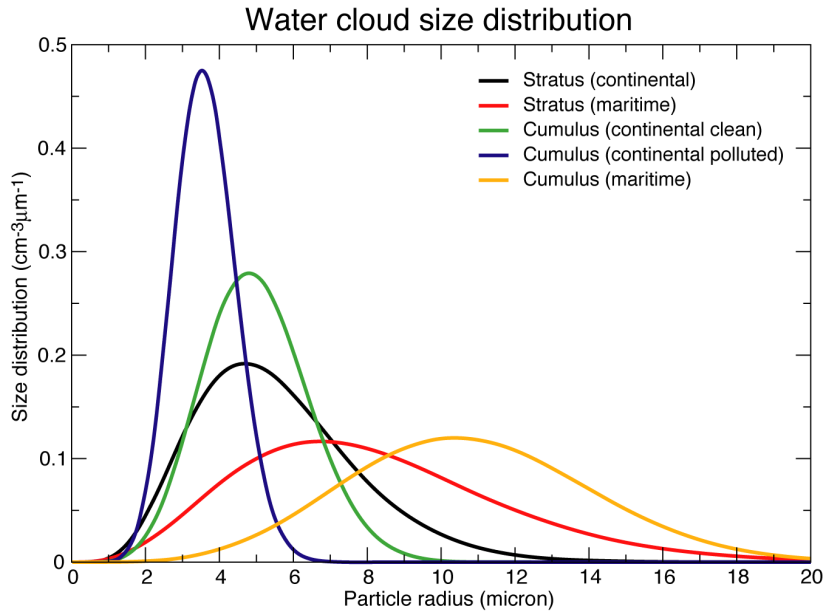


Figure 9 The normalized size distribution for the water cloud types.

A useful quantity often used in cloud research to describe the droplet size distribution is the effective radius r_{eff}

$$r_{eff} = \frac{\int_{r_{min}}^{r_{max}} r^3 n(r) dr}{\int_{r_{min}}^{r_{max}} r^2 n(r) dr} \tag{56}$$

The effective radius gives a measure of the droplet mean size. Since a spherical droplet scatters an amount of light proportional to its cross-sectional area, the effective radius differs from the simple mean radius in that the droplet cross section is used as a weight factor.

The microphysical properties for each cloud type are tabulated in Table 4. Note that we have included typical values of the particle number density, N (in units of cm⁻³), and the cloud liquid water content, LWC (in units of g m⁻³). If we assume that the droplet size distribution does not change, we can relate the particle number density and cloud liquid water content as follows:

$$LWC = \frac{4\pi}{3} \rho_l N \int_{r_{min}}^{r_{max}} r^3 n^l(r) dr \tag{57}$$

For a given atmospheric layer, the input provided by the user is the average value of the cloud liquid water content in the layer. The liquid water content is then internally converted by RTIASI into the average particle

density, N , using the scaling factor, S , computed from the values of N and LWC tabulated Table 4: $S = \frac{LWC}{N}$

For all water cloud models the lower, r_{min} , and upper, r_{max} , limit of particle size are set equal to $0.02 \mu\text{m}$ and $50 \mu\text{m}$ respectively.

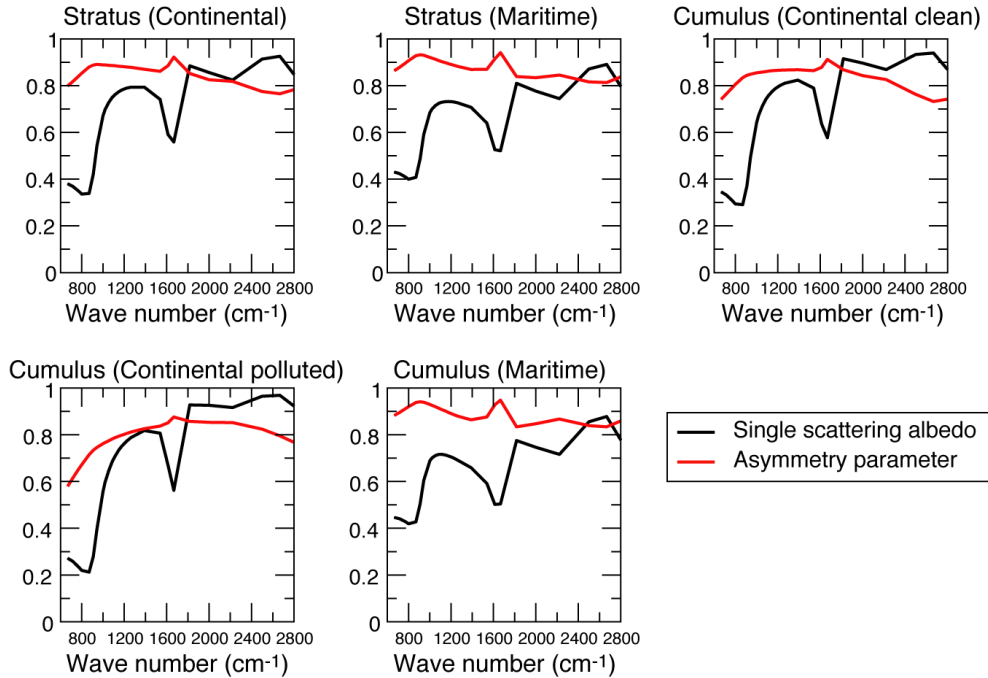


Figure 10 The single scattering albedo and asymmetry parameter for the five cloud types included in RTIASI-5.

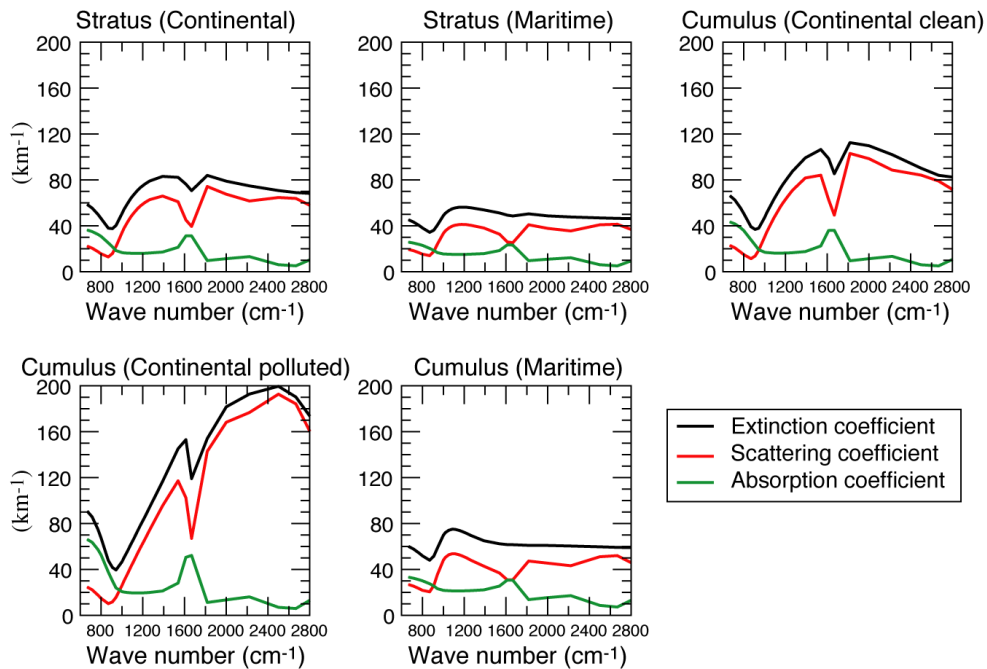


Figure 11 The absorption, scattering and extinction coefficient for the five cloud types included in RTIASI-5.

Analogous to the database of optical properties for aerosols, we have interpolated the water refractive indices to the central wavelength of each of the 8461 IASI channels and then generated a database of optical properties (absorption coefficient, scattering coefficient, extinction coefficient, phase function, asymmetry parameter, second moment of the phase function and the b parameter) for every single water cloud type using the Lorentz-Mie theory.

Cloud type	$r_{\text{mod}} (\mu\text{m})$	α	γ	a	$r_{\text{eff}} (\mu\text{m})$	$N(\text{cm}^{-3})$	$\text{LWC}(\text{g m}^{-3})$
Stratus (continental)	4.7	5	1.05	9.729E-3	7.33	250	0.28
Stratus (maritime)	6.75	3	1.30	3.818E-3	11.30	80	0.30
Cumulus (continental clean)	4.8	5	2.16	1.105E-3	0.0782	400	0.26
Cumulus (continental polluted)	3.53	8	2.15	8.119E-4	0.247	1300	0.30
Cumulus (maritime)	10.4	4	2.34	5.674E-5	0.00713	65	0.44

Table 4 The microphysical properties of the water clouds included in RTIASI-5.

The optical properties for the five water cloud types included in RTIASI-5 are plotted in Figures 10 and 11. For all cloud types the single scattering albedo in the shortwave is larger than the single scattering albedo in the longwave and with the exception of the Cumulus (continental polluted) type the asymmetry parameter also tends to increase with wave number. Also note the significantly larger values of the scattering and extinction coefficients for the Cumulus (continental polluted) type.

5. The dataset of optical properties for cirrus clouds

Cirrus clouds are made of ice crystals. The size and shape of ice crystals vary greatly from polar regions to midlatitudes to tropics. Typical shapes include bullet rosettes, hollow and solid columns, plates and aggregates. A typical shape often used in the literature is the hexagonal prism either in the form of column or plate. An exact solution for the interaction of a plane wave with a hexagonal ice crystal cannot be sought using the Lorentz-Mie theory. The problem is complicated by the fact that there is no practical solution that can be used to cover for all the crystal sizes that occur in the Earth's atmosphere. For the case when the size of an ice crystal is much larger than the wavelength of the incident radiation the only practical approach to solve the problem of light scattering is the Geometric Optics (GO) method (Takano and Liou 1989). The GO method is based on the assumption that a light beam is made of a bundle of parallel rays that undergo reflection and refraction outside and inside the crystal. The directions of propagation are determined using the Snell law at the surface of the crystal and the total field is made of the diffracted rays plus the reflected and refracted rays. For the problem of light scattering by small ice crystals a number of methods have been developed such as the Finite-Difference Time domain Method (FDTD) (Yang and Liou 1996) and the Direct Dipole Approximation (DDA) (Draine and Flatau 1994). An inherent shortcoming of these methods is that they are computationally expensive to the extent that they can become impractical if a solution is sought for randomly oriented particles. The most effective method for calculations of light scattering by small ice crystals is probably the T-matrix (Mishchenko et al. 2000) that relates the incident and scattered fields by means of a T-matrix after they have been expanded in terms of spherical wave functions.

For RTIASI-5 we have generated a composite database of optical properties for hexagonal ice crystals randomly oriented in space using the GO method for large crystals and the T-matrix method for small crystals. The publicly available codes developed by Macke et al. (1996) and Kahnert (2004) have been used respectively. The GO code uses the Monte Carlo method for geometric ray tracing and includes the

contribution of absorption. The total phase function computed using the GO technique is a combination of the ray-tracing phase function and the Fraunhofer diffraction component. The standard GO method produces a ray-tracing phase function with a strong and narrow peak in the forward scattering direction. This effect is an artefact of the GO technique that ignores physical optics effects and is known as δ -function transmission (Takano and Liou 1989). To reconcile the approximated GO results with exact results and produce a phase function with an angular profile similar to the diffraction component we have modified the GO code applying the methodology described in Mischenko and Macke (1998). Modifications to the GO code were also made to make it possible to compute the phase function at a number of non evenly spaced angles.

Convergent results for the T-matrix code could only be obtained for the smaller and less elongated hexagonal columns. In fact part of the numerical procedure associated with the T-matrix method is a numerical matrix inversion. This can become an ill-conditioned problem that leads to non-convergent results if the size of the matrix is too large as in the case of the larger columns when a high number of expansion orders is needed to expand the electromagnetic fields. The wavelength range covered by each technique is given in Table 5.

Crystal length (μm)	Method	Wavelength
4	T-matrix	Whole IASI spectrum
7.5	T-matrix	Whole IASI spectrum
15	T-matrix	Whole IASI spectrum
25	T-matrix	Whole IASI spectrum
35	T-matrix	Whole IASI spectrum
45	T-matrix	$\geq 5\mu\text{m}$
45	GO	$<5\mu\text{m}$
60	T-matrix	$\geq 6\mu\text{m}$
60	GO	$<6\mu\text{m}$
80	T-matrix	$\geq 11\mu\text{m}$
80	GO	$<11\mu\text{m}$
100	T-matrix	$\geq 14\mu\text{m}$
100	GO	$<14\mu\text{m}$
130	GO	Whole IASI spectrum

Table 5 The wavelength range covered by the GO and T-matrix method.

For cirrus clouds, the size distribution used in this paper is from Heymsfield and Platt (1984). It covers eight different temperature ranges from -20C to -60C and crystal sizes less than $20\mu\text{m}$. To account for the radiative effect due to the presence of small ice crystals, the Heymsfield and Platt distribution has been extrapolated to $4\mu\text{m}$ using the method described in Mitchell et al. (1996). To better resolve the structure of the spectra we have discretized the size distribution into 24 bins. The midpoint crystal length varies from $4\mu\text{m}$ to $3500\mu\text{m}$ as shown in Table 6.

		Crystal length (:m)										
4	7.5	15	25	35	45	60	80	100	130	175	225	
275	350	450	550	650	750	900	1150	1400	1750	2500	3500	

Table 6. The length of the hexagonal crystals used in RTIASI-5.

The absolute value of the size distribution for the eight temperature ranges is plotted in Figure 12. It is evident how the magnitude of the size distribution is significantly smaller for the lower temperatures.

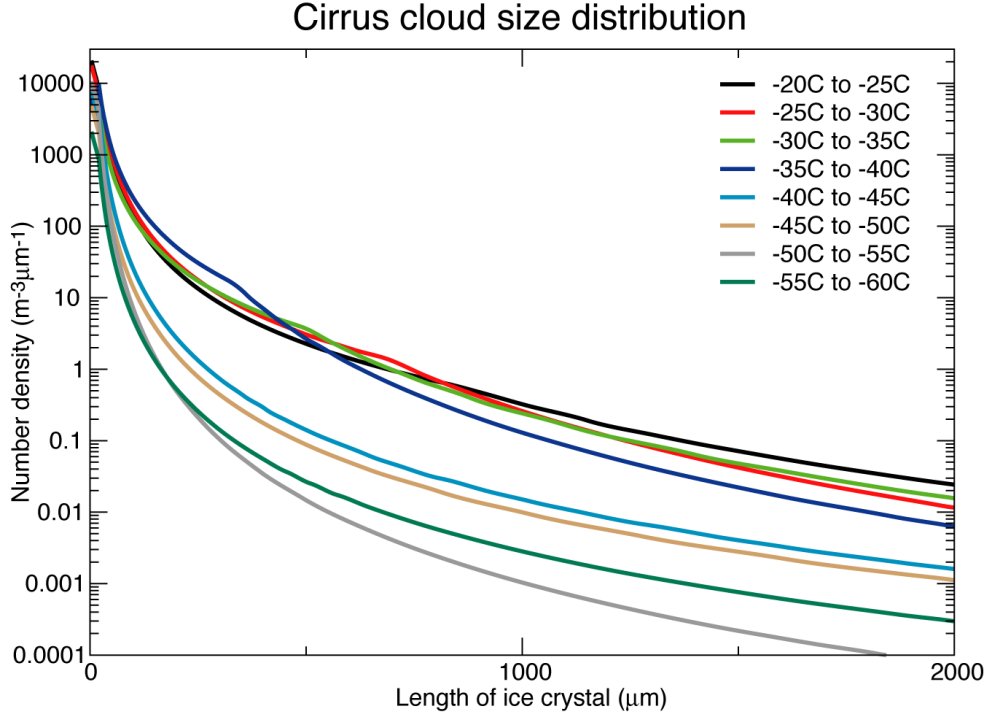


Figure 12 The absolute value of the size distribution for the cirrus cloud types included in RTIASI-5.

The width, D , of the crystal has been derived from the length, L , of the crystal using the aspect ratio given in Yang et al. (2003)

$$\frac{D}{L} = \begin{cases} 1 & L \leq 40 \mu m \\ \exp(-0.017835(L - 40)) & 40 < L \leq 50 \mu m \\ \frac{5.916}{\sqrt{L}} & L > 50 \mu m \end{cases} \quad (58)$$

For a given atmospheric layer, the input provided by the user is the average value of the ice water content in the layer, IWC . If we assume that the ice crystal size distribution does not change, we can relate the particle number density and ice water content as follows:

$$IWC = \rho_i N \int_{r_{min}}^{r_{max}} V(L) n^1(L) dL \quad (59)$$

where V is the volume of the hexagonal ice crystal, L is the maximum dimension (length) of the crystal and ρ_i is the density of ice. The average particle density can then be obtained using the scaling factor, S , computed from the values of N and IWC in Table 7: $\frac{IWC}{N}$.

For each ice crystal size distribution we can define, analogous to the water droplet effective radius, a mean effective size, D_e , obtained by taking the ratio of the volume-weighted to the area-weighted size distributions

$$D_e = \frac{\int_{L_{\min}}^{L_{\max}} D^2 L n(L) dL}{\int_{L_{\min}}^{L_{\max}} D L n(L) dL} \quad (60)$$

The values of the effective size for the ice crystal size distributions used in this paper are tabulated in Table 7.

Temperature range	N (cm ⁻³)	IWC (g m ⁻³)	D_e (μ m)
-20° to -25°	0.3448	0.020885	92.4
-25° to -30°	0.4029	0.021794	82.2
-30° to -35°	0.1989	0.020221	97
-35° to -40°	0.4234	0.023646	74.8
-40° to -45°	0.1675	0.002323	51.6
-45° to -50°	0.0816	0.001344	56.2
-50° to -55°	0.1144	0.000625	32.9
-55° to -60°	0.0339	0.000452	50.6

Table 7 The particle number density, ice water content and effective size for the cirrus cloud types included in RTIASI-5.

The refractive indices of ice are important parameters in the computation of the scattering and absorption properties of ice crystals. In this study real refractive indices compiled by Warren (1984) are used for all wavelengths covered by IASI. Complex refractive indices compiled by Warren were also used for wavelengths longer than 7.8 μm. For wavelengths shorter than 7.8 μm more recent values of the complex refractive indices compiled by Gosse et al. (1996) have been used. In this spectral range they can differ from the ones compiled by Warren by as much as 30%. In the IASI spectral range, refractive indices for ice are tabulated at 89 different frequencies. Given the computational time required to perform the GO and T-matrix computations, the procedure of interpolating the refractive indices to the IASI central frequencies and then perform the GO and T-matrix computations for each IASI channel is impractical. We have instead performed computations for each of the 89 tabulated refractive indices and then interpolated the results to each IASI channel. Since the refractive indices for ice are a slowly varying function of the wavelength, for any practical purpose we can consider the ice crystal optical properties to be constant over the width of an IASI channel.

To generate the database of optical properties for randomly oriented ice crystals we have firstly computed the optical properties (absorption coefficient, scattering coefficient, extinction coefficient, phase function at 208 angles, asymmetry parameter and second moment of the phase function) for every single hexagonal crystal using the crystal length and crystal width specified in Table 6 and Eq. (58), respectively. To obtain the optical properties for a sample of ice crystal particles we have then applied Eqs. (46), (47), (48) and (49) using the modified Heymsfield and Platt size distributions.

The T-matrix computations have required quite an involving stage of pre-processing. For a given crystal geometry the T-matrix code is in fact not designed to give automatically convergent results. The expansion orders needed to obtain convergent results (within a given accuracy) for a particular crystal size and frequency had in fact to be determined by trial and error since no guidance was available for the geometries and refractive indices involved in this exercise.

The optical properties for a selected number of temperature range is plotted in Figures 13 and 14. As a result of the phase function strong and narrow peak in the forward direction, the asymmetry parameter is consistently larger than 0.9 across the whole spectral range. The single scattering albedo tends to increase with wave number and the optical thickness of the cloud decreases dramatically with lower temperatures.

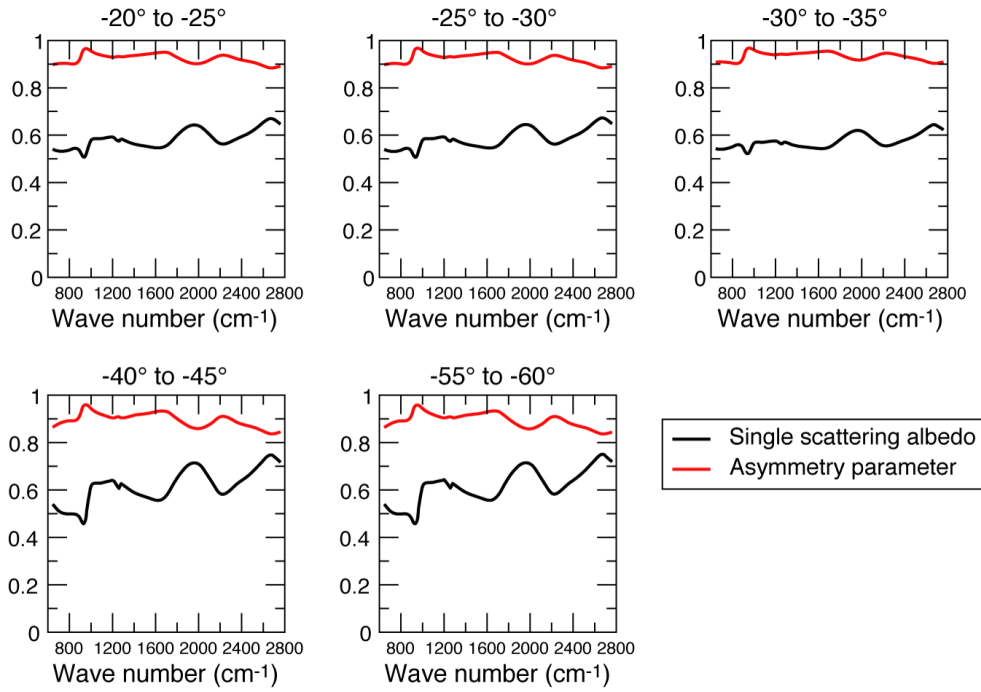


Figure 13 The single scattering albedo and asymmetry parameter for a selected number of cirrus cloud types included in RTIASI-5.

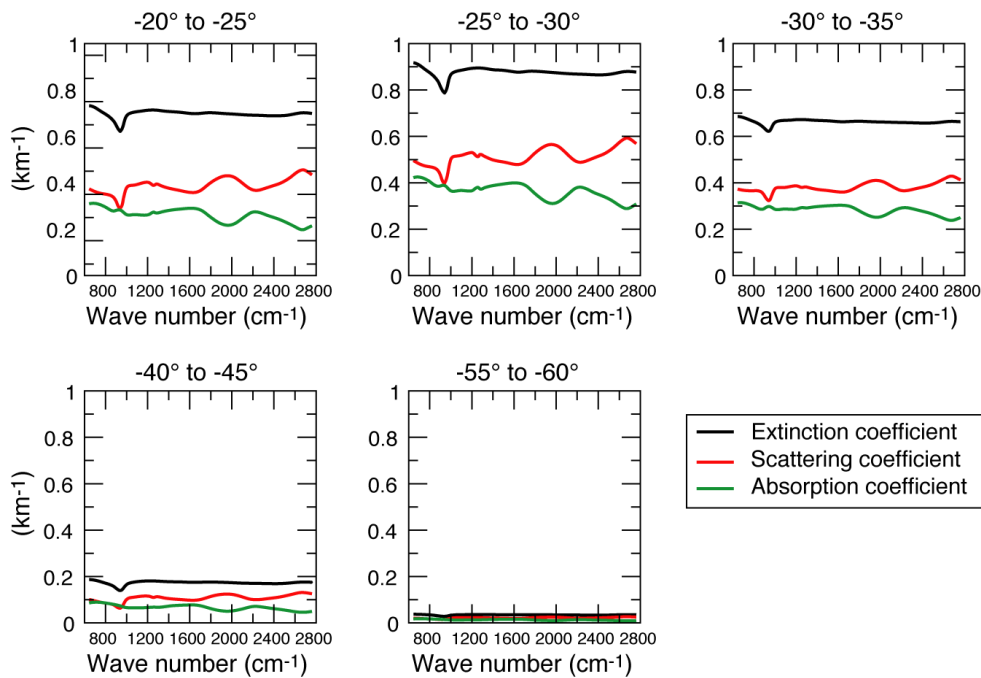


Figure 14 The absorption, scattering and extinction coefficient for a selected number of cirrus cloud types included in RTIASI-5.

It should be mentioned that the optical properties used in RTIASI-5 for aerosols, water clouds and cirrus clouds have been obtained on the basis of microphysical properties that, given their highly variable nature, do not necessarily reflect an actual situation. For this reason, RTIASI-5 allows the user to externally specify the values of the optical properties used in the radiative transfer. Finally, in Appendix A we give a brief summary of the input profile configuration required by RTIASI-5 to perform multiple scattering computations in presence of aerosols and clouds. More specific details can be found in the RTIASI-5 user's guide.

6. The stream method

In RTIASI-5, the radiative transfer equation applies to plane-parallel atmospheres (i.e. horizontally homogeneous). For an atmosphere where a number of layers are partially covered by clouds we have to address the problem of the radiative transfer for a horizontally non-homogeneous atmosphere. A rigorous approach to this complicated problem is well outside the scope of this report and we have to resort to approximate solutions. A widely used approach is the reduction of a partly cloudy layer to an equivalent homogeneous layer. This is achieved by re-distributing the optical thickness of the cloud over the entire layer in such a way that the reflectance of the cloud is the same as the one for the partly cloudy layer. The implementation of this technique would require a non-opaque cloud with fractional cover CFR to be treated as an opaque cloud (i.e. a black body) with an effective cloud fraction equal to CFR times the emissivity of the cloud. This method has been found to generate results that are very sensitive to the vertical resolution (Raisanen 1998) and by its intrinsic nature we expect it to degrade the accuracy of the radiance computation. The alternative approach is to divide the atmosphere into a number of homogeneous columns, each column containing either cloud-free layers or totally cloudy layers. Despite being potentially more accurate, this technique (henceforth referred to as "stream method") has seldom been exploited (Amorati and Rizzi 2002) since depending on the number of layers and the overlapping assumption, the number of columns can become so large that it is impractical to use when lower orders approximations are used for multiple scattering (i.e two stream method). However, given the nature of the multiple scattering parameterization used in RTIASI-5, the computational burden of the stream method is only a fraction of the total and consequently we have implemented it in RTIASI-5. Note that preliminary results obtained from data collected during a number of field campaigns (Rizzi 2004) suggest that radiances computed using the stream method are in better agreement with measurement than those computed using the grey cloud approach.

To describe the stream method we give here an example where seven atmospheric layers are considered. The cloud parameters in each layer are shown in Figure 15.

Layer	Cloud fractional coverage (%)
1	0
2	50
3	0
4	30
5	80
6	0
7	0

Figure 15 The cloud fractional coverage in each layer

In what follows, the cloud coverage represents the fraction of the instrument Field of View (FOV) covered by the cloudy layer. With reference to Figure 15, starting from the top of the atmosphere (layer 1), the cloud

In the context of the stream model, the clear sky radiance can include the effect of aerosols. In fact, in RTIASI-5 the user can define a mixture of clouds and aerosols in each layer. The presence of aerosols will not affect the number of streams and the area coverage but will affect the radiative properties of the stream. Note that in RTIASI-5 the user is not allowed to place two different cloud types on the same layer (i.e. the optical properties for a combination of different cloud types will not be computed). If this happens, RTIASI-5 will return an error message and the execution of the program will be stopped.

7. Results

The accuracy of the scaling approximation has been studied by comparing the approximate solution given by Eqs. (38), (39) and (40) with reference results obtained using a doubling-adding algorithm. The doubling-adding method is a very efficient and accurate way of solving numerically the problem of multiple scattering. Results shown in this paper have been obtained by adapting to the infrared the code originally developed by Bauer (2002) for the microwave. The anisotropy of the radiance fields in the infrared is stronger than in the microwave and so in principle a larger number of quadrature points (streams) are required. For this study we found that a degree of accuracy well below the IASI instrument noise can be achieved by using 42 streams. Approximate and reference radiances for the IASI channels have been obtained by performing the convolution of high-resolution monochromatic radiances. To this end we have used line-by-line optical depths for the molecular species. For aerosols and clouds we have used optical depths from the respective databases assuming the optical depth is constant within the width of a channel.

As mentioned in section 2, a resolution of 0.001cm^{-1} is in principle required for the monochromatic radiances. However, the process of computing doubling-adding monochromatic radiances at this resolution is so time consuming to render its execution prohibitive. Since the line-by-line optical depths are truly monochromatic quantities we have re-sampled the spectra at the lower resolution of 0.05 cm^{-1} . The study we carried out to develop the first version of RTIASI has shown that the use of a lower resolution spectrum degrades the radiance accuracy to above the noise level for the channels with weighting functions peaking in the upper troposphere/lower stratosphere since, to resolve the typical width of a line, a resolution not lower than 0.001 cm^{-1} is required. However, one should note that these channels are the least affected by the presence of clouds and aerosols. Moreover, we are not interested here in the absolute value of the radiance but rather in the relative difference between radiances. On this basis we can consider the following results to give a fairly accurate estimate of the errors introduced by the scaling approximation.

In what follows the accuracy of the scaling approximation is expressed in terms of the difference between approximated and reference spectra obtained by including in the radiative transfer each of the RTIASI-5 aerosol and cloud types. Note that all results do not include the errors introduced by the transmittance parameterization used in RTIASI-5. Finally, to assess the impact of each aerosol/cloud type on the top of the atmosphere radiance we have also computed the difference between clear-sky and reference spectra.

7.1 The results for aerosols

For each aerosol type we have computed spectra for a tropical and arctic profile selected from the 117 independent profile data set (profiles number 1 and 36 respectively). To obtain the vertical profile for each aerosol type we have applied the methods described in Hess et al. (1998). Here we briefly mention that the surface number densities tabulated in Table 3 have been extrapolated to 35 km assuming the atmosphere is divided up into three layers. The first one represents the planetary layer, the second one represents the free troposphere and the third one is the stratospheric layer. The upper boundary of the planetary layer is placed

at 2km with the exception of the Desert and Antarctic aerosol types for which the top of the layer is placed at 6 and 10 km respectively. The top of the free troposphere is always placed at 12 km and the stratosphere extends up to 35 km. The variation of the number densities with altitude is described by an exponential profile and a background concentration profile is assumed in the free troposphere and the stratosphere irrespective of the aerosol type. The number densities tabulated in Table 3 are representative of global average conditions. To represent more extreme cases, we have computed a number of additional spectra assuming a value of the number density four times the global average value. Results are plotted in Figures 17 to 34. The top and bottom panels show results for the global average and extreme conditions respectively.

The desert aerosol type has by far the largest impact on the radiance. Figure 25 shows that for the extreme condition case the presence of desert dust in a tropical profile can result in a reduction of the top of the atmosphere radiance by 4K in the thermal infrared and by 1.8K in the short wave. Smaller differences are observed for the average condition case and in general for the arctic profile (Figure 26). Errors introduced by the scaling approximation are less than 1K in the thermal infrared and less than 0.25 K in the short wave. The Urban aerosol type is the next in order of importance in terms of radiance attenuation (Figures 23 and 24). For the extreme condition case the radiance attenuation can be as large as 1 K in the thermal infrared and 0.6 K in the short wave. For the average concentration case the radiance attenuation is typically less than 0.2 K across the whole spectrum. For the other aerosol types a smaller radiance attenuation is observed; this seldom exceeds 0.1 K for the average condition case and 0.5 K for the extreme condition case. For all aerosols types the radiance attenuation is larger in the thermal infrared than in the short wave. This is a consequence of the fact that the effective transmittance in Eq (35) is smaller in the short wave and this renders the atmosphere more transparent to aerosols.

Errors introduced by the scaling approximation are typically small. For the Urban type these never exceeds 0.1 K whereas for the other aerosol types they are typically below 0.05 K. For all aerosol types, errors observed in the thermal infrared are larger than the ones observed in the short wave. In fact the scaling factor b in Eq (35) is smaller in the short wave. This implies that more radiation is scattered in the forward direction (i.e the asymmetry parameter g is closer to 1) and in the limit of $b \rightarrow 0$ ($g \rightarrow 1$) we expect the reference and approximate radiances to converge since in this case the attenuation of the radiance becomes only due to absorption.

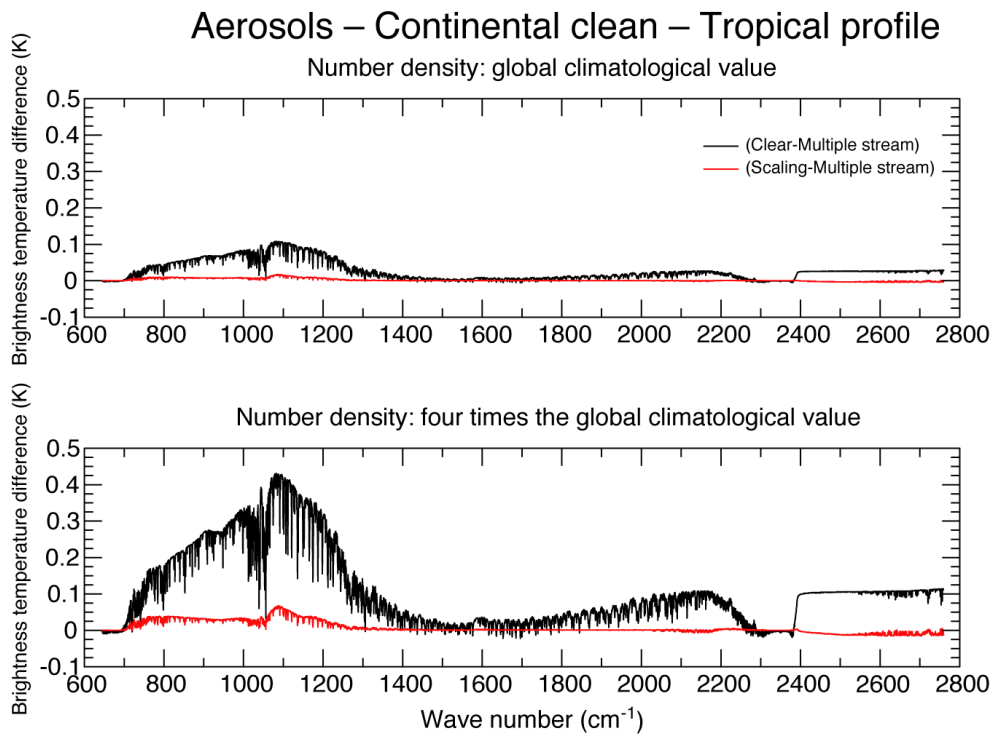


Figure 17 The radiative impact of the Continental Clean aerosol type (black curve) and the error introduced by the scaling approximation (red curve) for the tropical profile for two different aerosol number densities.

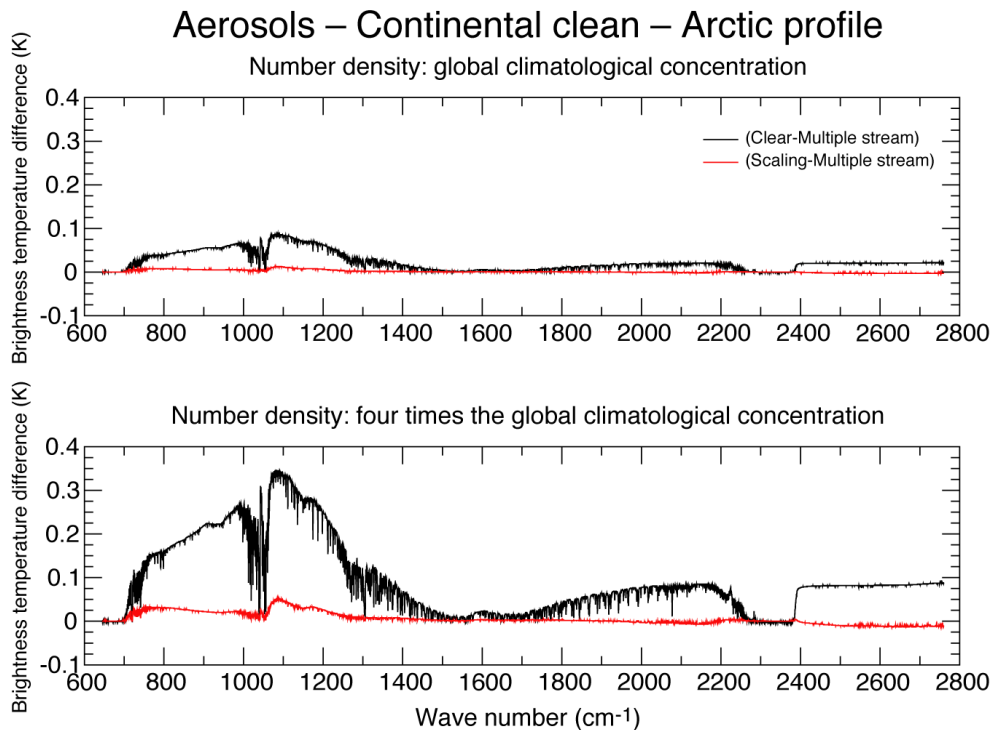


Figure 18 The radiative impact of the Continental Clean aerosol type (black curve) and the error introduced by the scaling approximation (red curve) for the arctic profile for two different aerosol number densities.

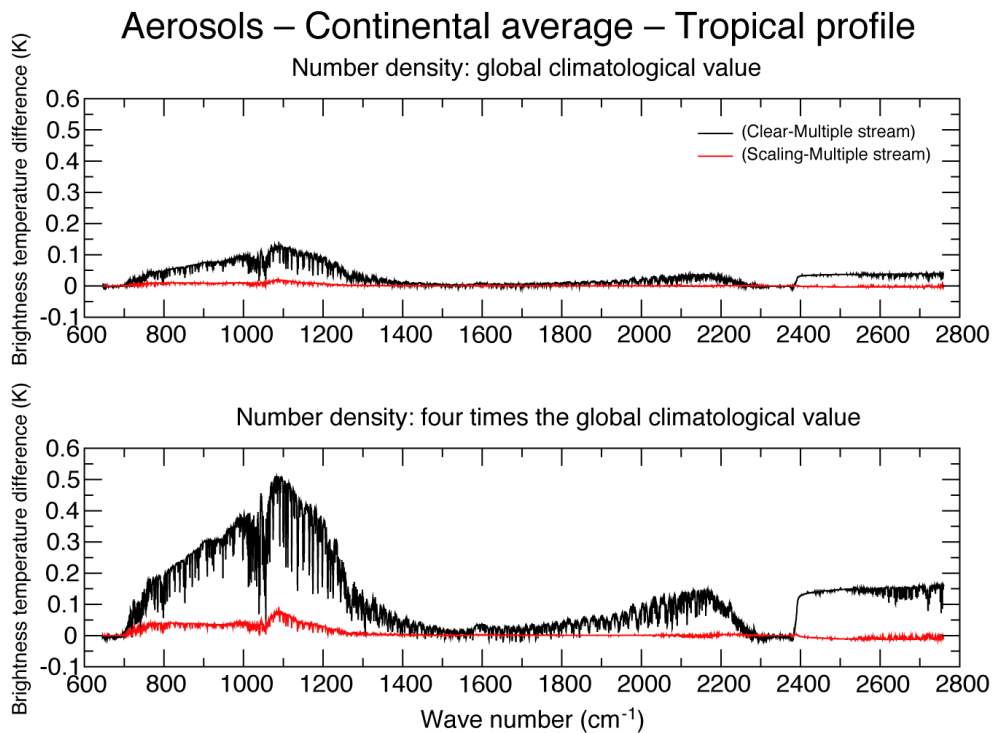


Figure 19 The radiative impact of the Continental Average aerosol type (black curve) and the error introduced by the scaling approximation (red curve) for the tropical profile for two different aerosol number densities.

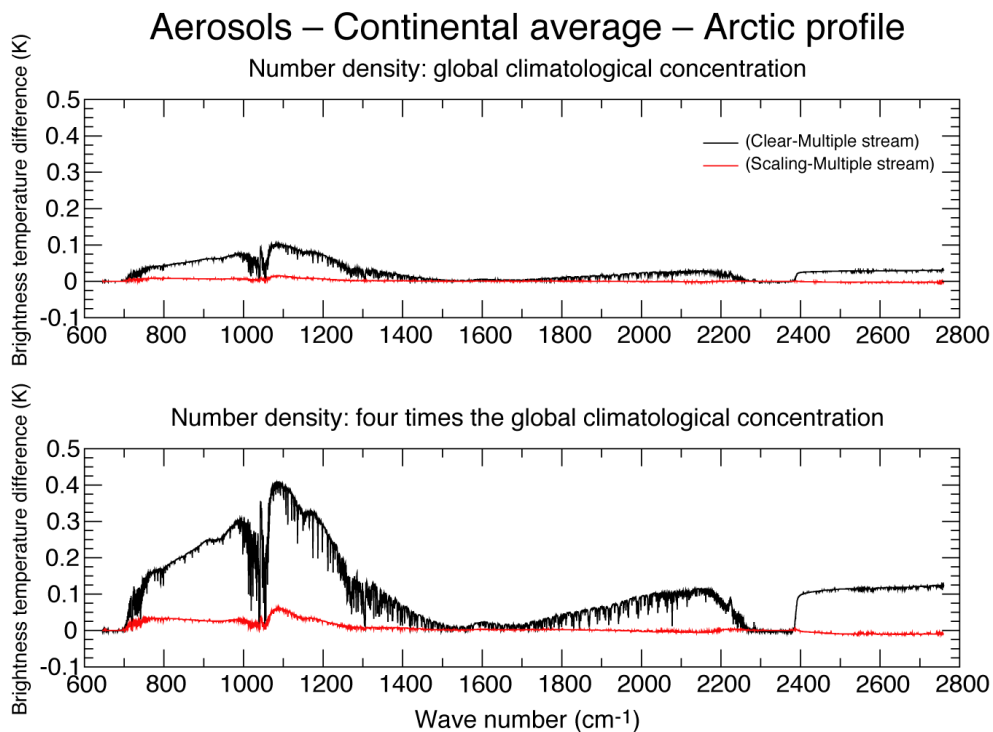


Figure 20 The radiative impact of the Continental Average aerosol type (black curve) and the error introduced by the scaling approximation (red curve) for the arctic profile for two different aerosol number densities.

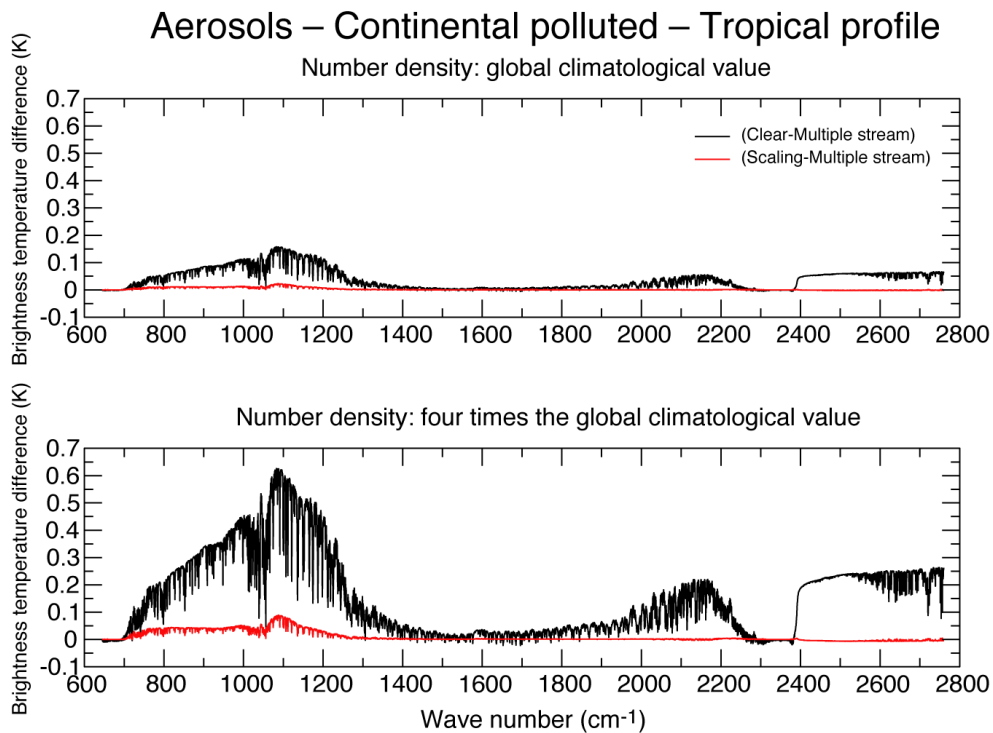


Figure 21 The radiative impact of the Continental Polluted aerosol type (black curve) and the error introduced by the scaling approximation (red curve) for the tropical profile for two different aerosol number densities.

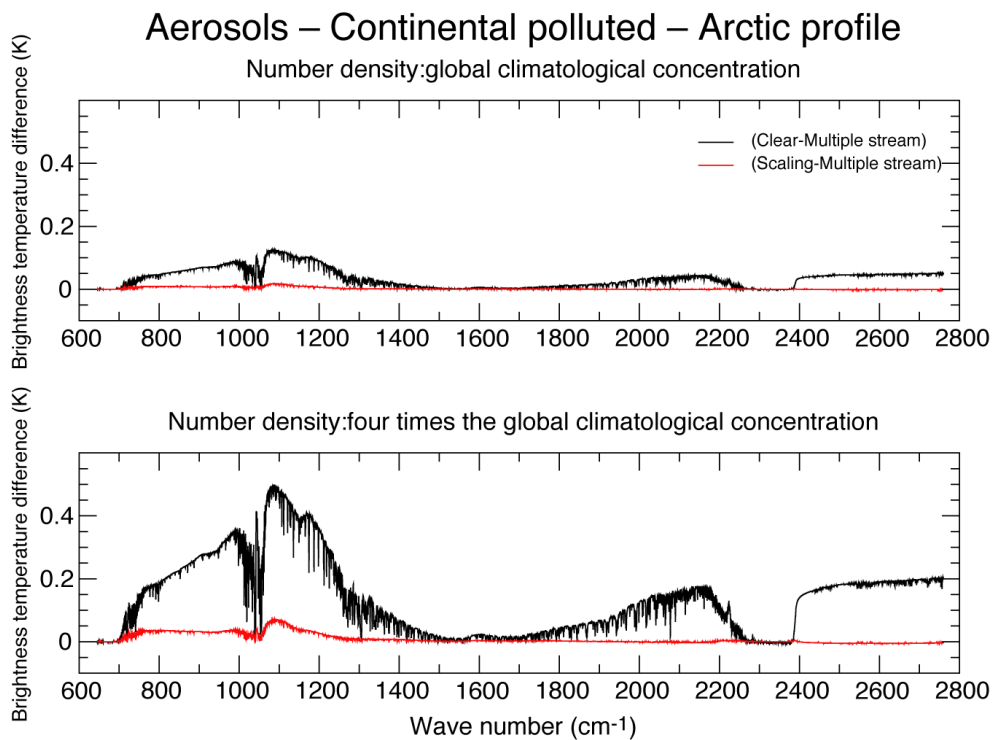


Figure 22 The radiative impact of the Continental Polluted aerosol type (black curve) and the error introduced by the scaling approximation (red curve) for the arctic profile for two different aerosol number densities.

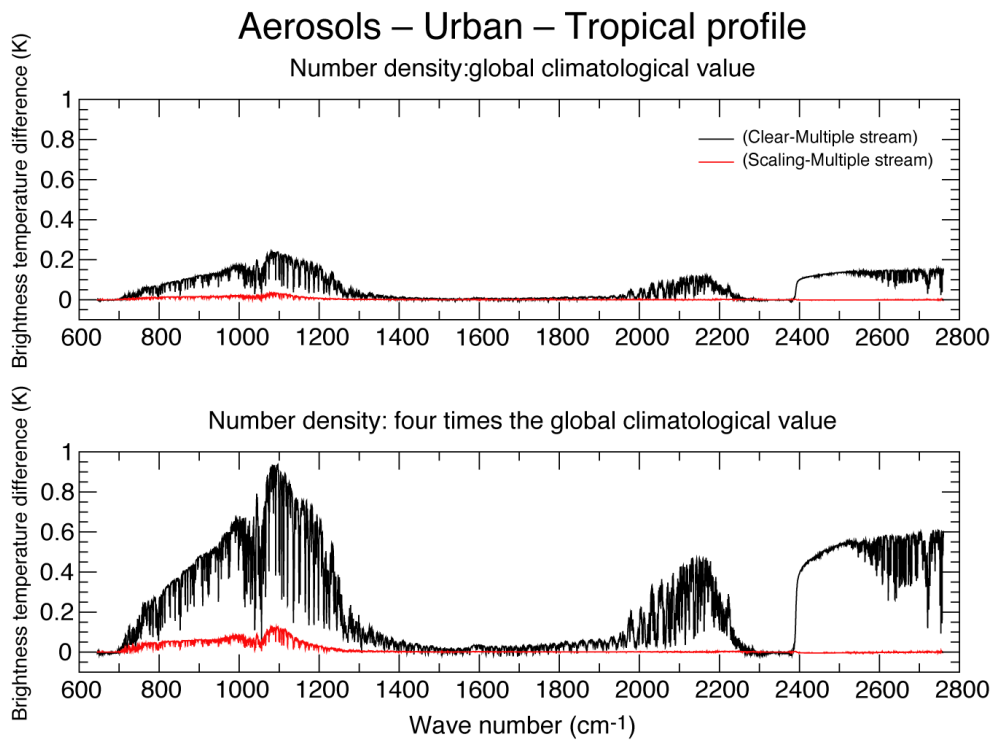


Figure 23 The radiative impact of the Urban aerosol type (black curve) and the error introduced by the scaling approximation (red curve) for the tropical profile for two different aerosol number densities.

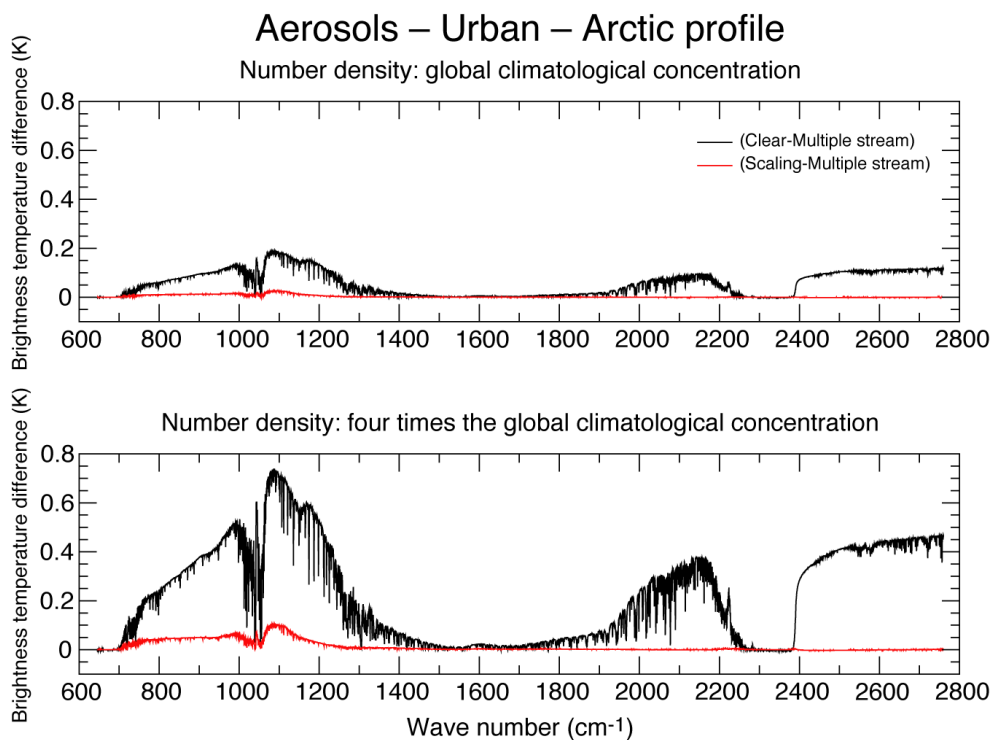


Figure 24 The radiative impact of the Urban aerosol type (black curve) and the error introduced by the scaling approximation (red curve) for the arctic profile for two different aerosol number densities.

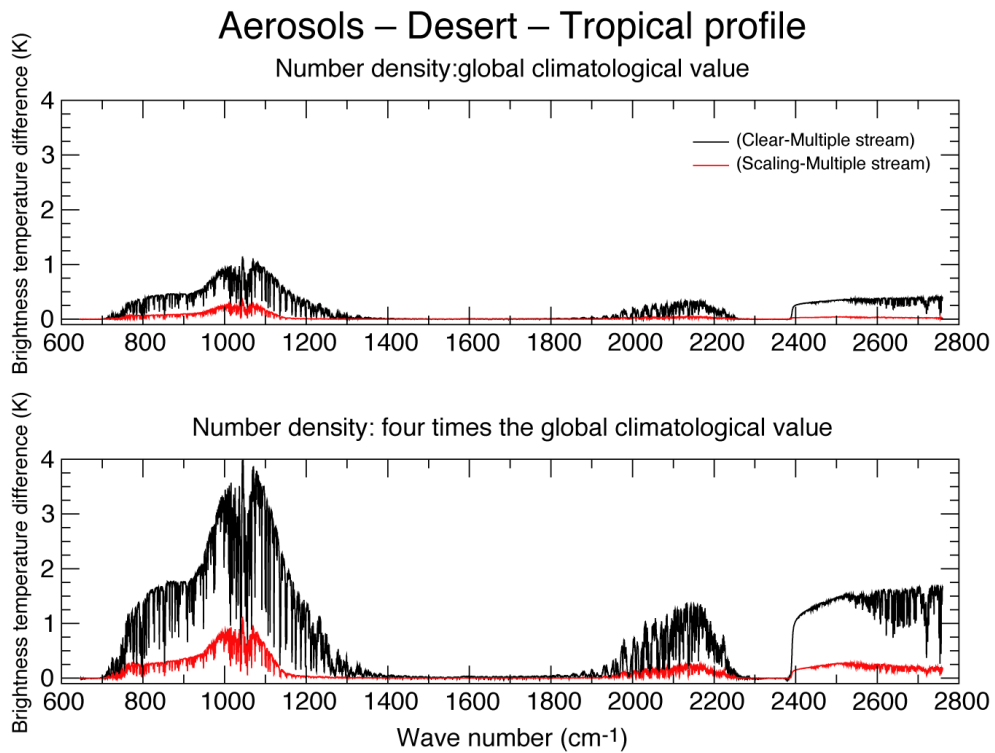


Figure 25 The radiative impact of the Desert aerosol type (black curve) and the error introduced by the scaling approximation (red curve) for the tropical profile for two different aerosol number densities.

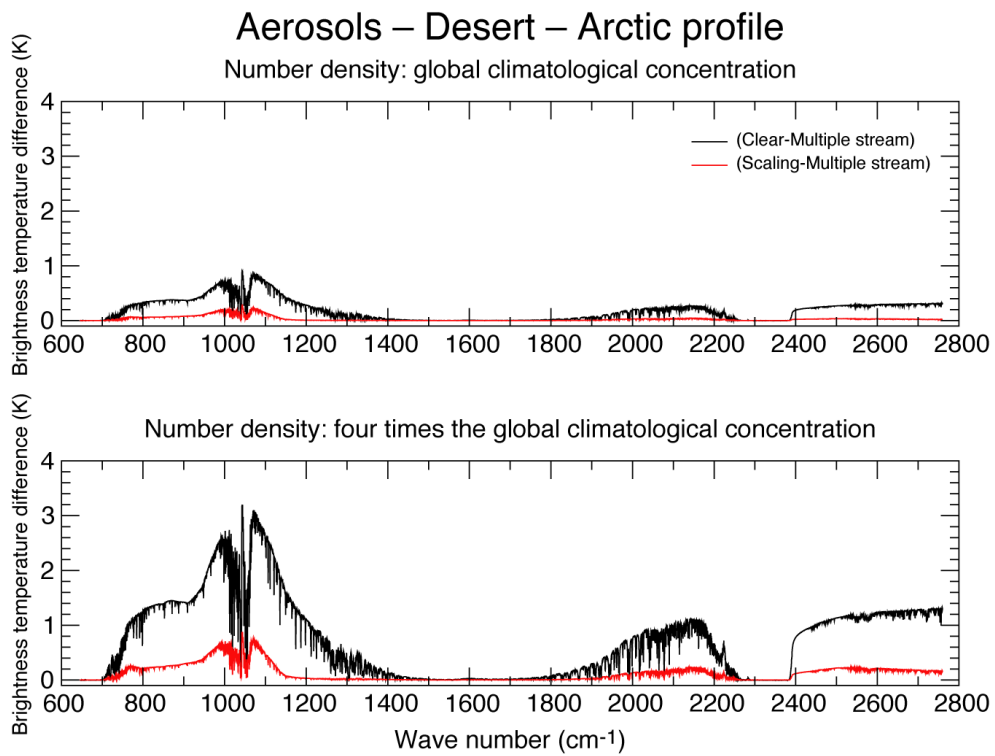


Figure 26 The radiative impact of the Desert aerosol type (black curve) and the error introduced by the scaling approximation (red curve) for the arctic profile for two different aerosol number densities.

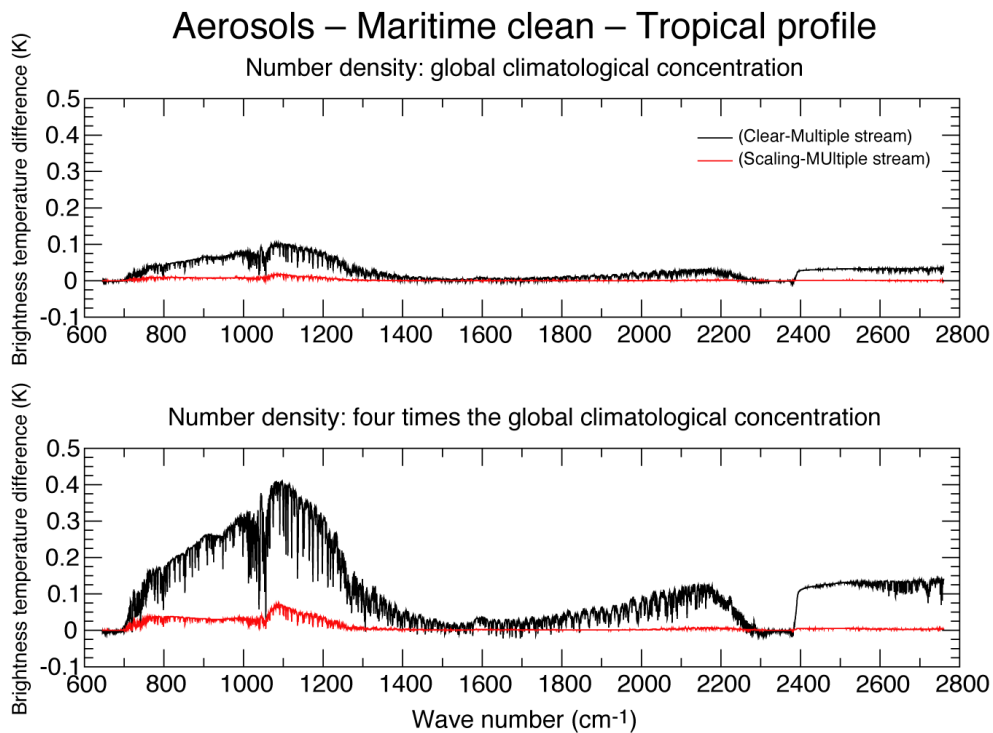


Figure 27 The radiative impact of the Maritime Clean aerosol type (black curve) and the error introduced by the scaling approximation (red curve) for the tropical profile for two different aerosol number densities.

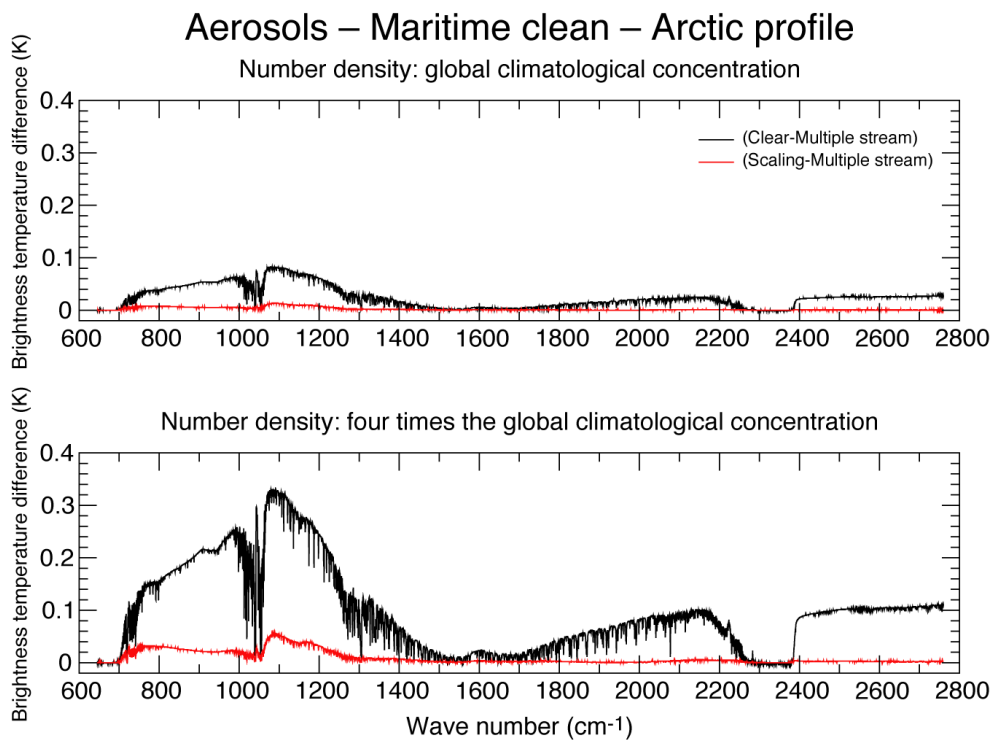


Figure 28 The radiative impact of the maritime Clean aerosol type (black curve) and the error introduced by the scaling approximation (red curve) for the arctic profile for two different aerosol number densities.

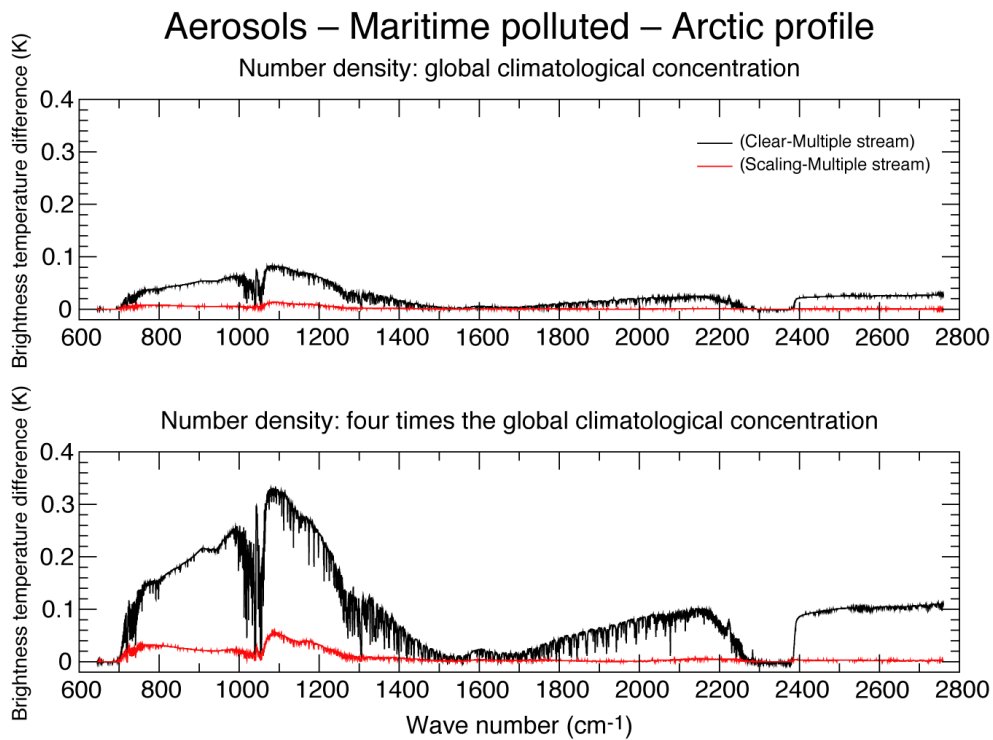


Figure 29 The radiative impact of the Maritime Polluted aerosol type (black curve) and the error introduced by the scaling approximation (red curve) for the tropical profile for two different aerosol number densities.

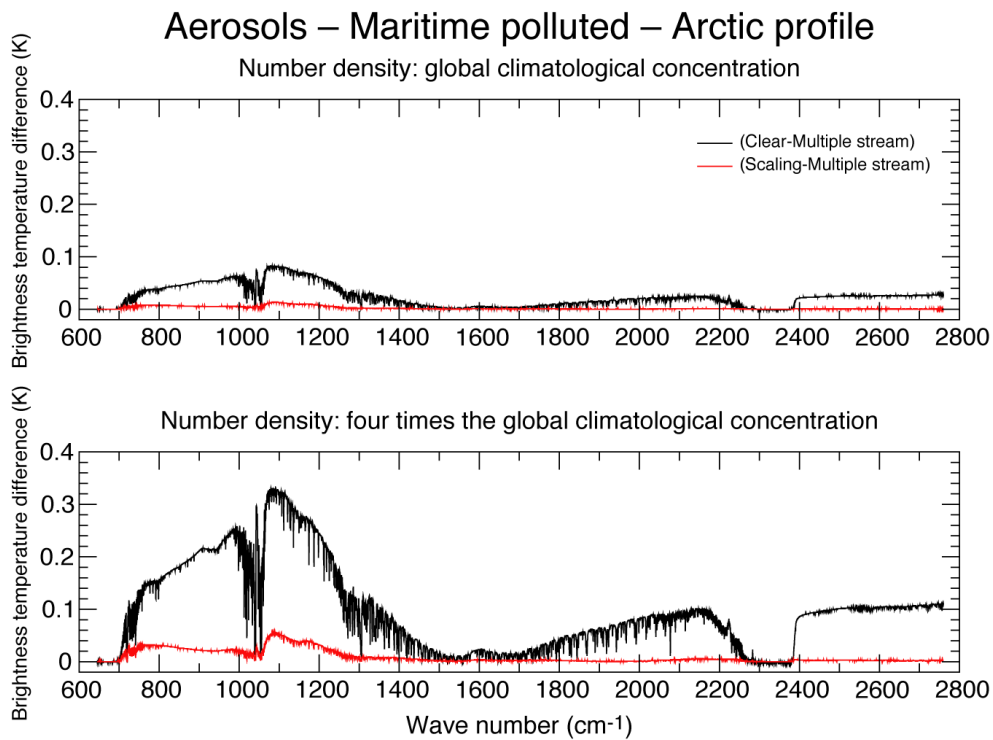


Figure 30 The radiative impact of the Maritime Polluted aerosol type (black curve) and the error introduced by the scaling approximation (red curve) for the arctic profile for two different aerosol number densities.

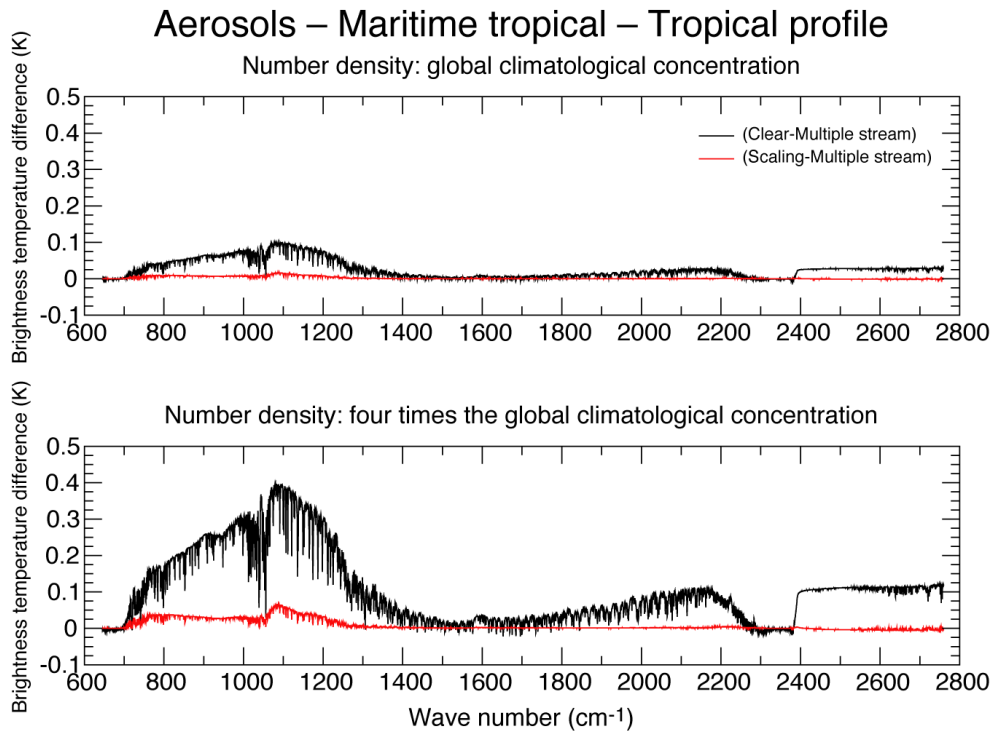


Figure 31 The radiative impact of the Maritime Tropical aerosol type (black curve) and the error introduced by the scaling approximation (red curve) for the tropical profile for two different aerosol number densities.

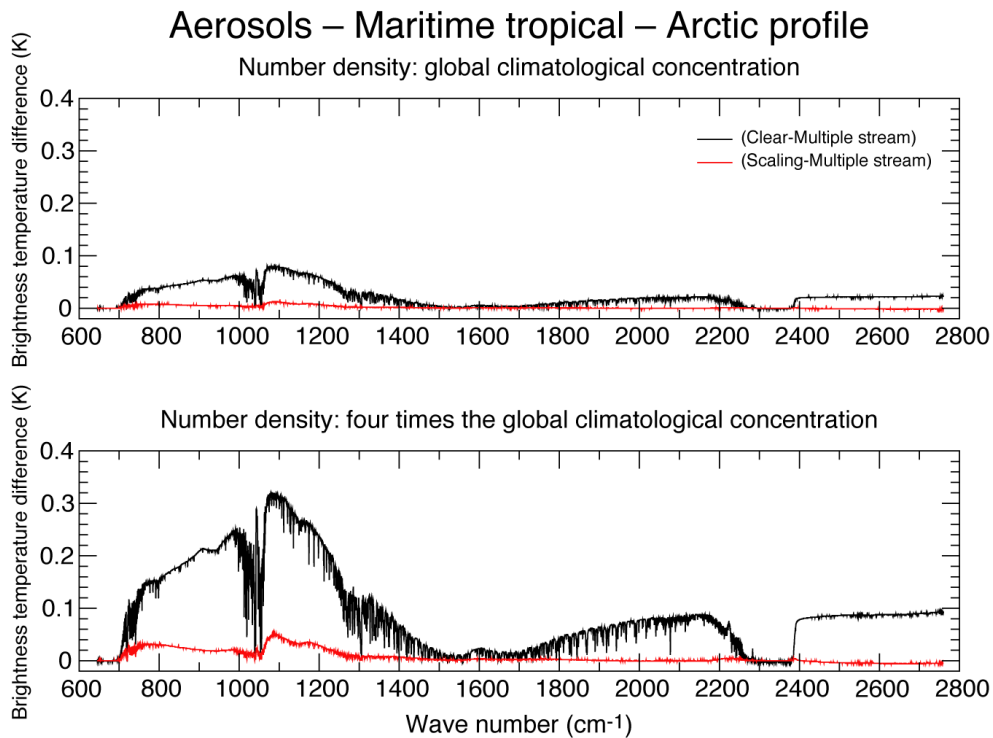


Figure 32 The radiative impact of the Maritime Tropical aerosol type (black curve) and the error introduced by the scaling approximation (red curve) for the arctic profile for two different aerosol number densities.

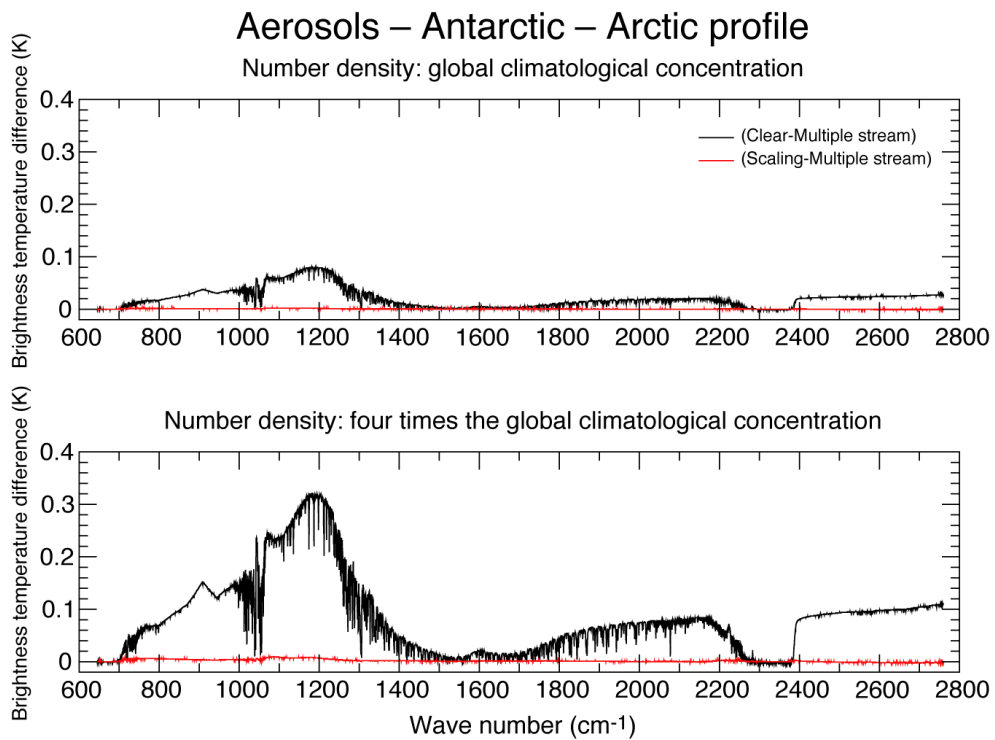


Figure 33 The radiative impact of the Antarctic aerosol type (black curve) and the error introduced by the scaling approximation (red curve) for the arctic profile for two different aerosol number densities.

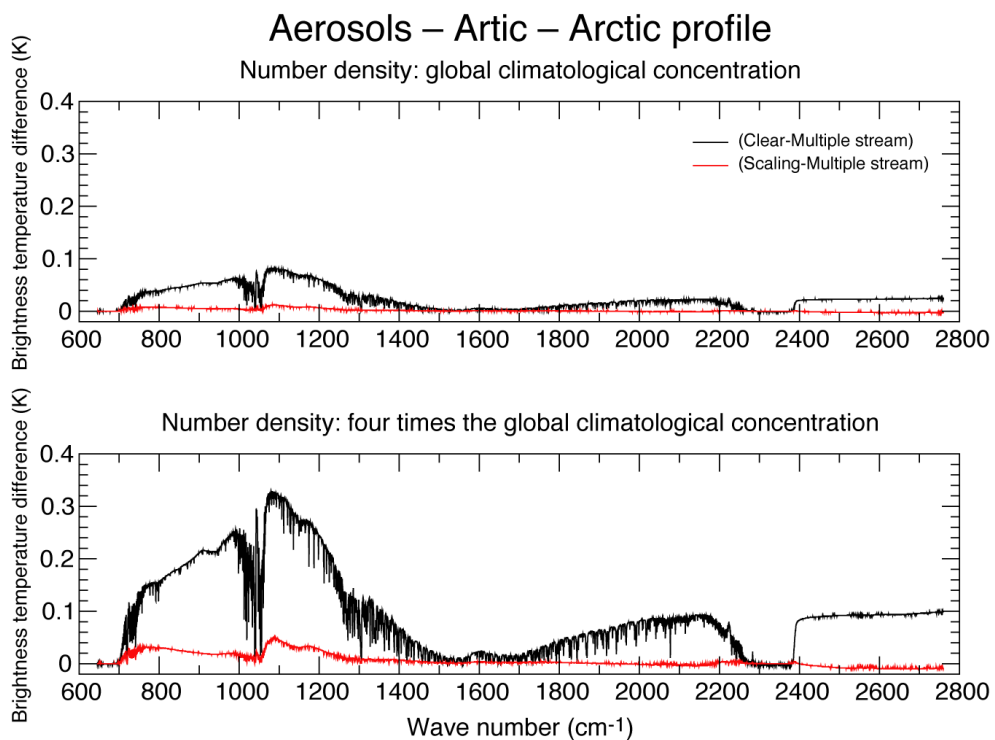


Figure 34 The radiative impact of the Arctic aerosol type (black curve) and the error introduced by the scaling approximation (red curve) for the arctic profile for two different aerosol number densities.

7.2 The results for water clouds

Results for the Stratus Continental type are shown in Figure 35 for the tropical profile and Figure 36 for the arctic profile. It is evident that the radiance attenuation is only significant in the more transparent spectral regions and channels whose weighting functions peak above the cloud are not influenced by the presence of the cloud. This is reflected in the different magnitude of the radiance attenuation for the tropical and arctic profile. The radiance attenuation resulting from the introduction of the cloud is larger in the shortwave and can reach 16 K for the tropical profile and 11 K for the arctic profile. No appreciable difference can be observed when the cloud thickness is doubled, thus suggesting that the cloud is rendered opaque by extinction. The error introduced by the scaling approximation for the tropical profile is less than 1 K in the thermal infrared and can be as large as 5 K in the short wave. Smaller values are observed for the arctic profile. Note that the error behaviour displays a pattern that is opposite that observed for the aerosol case. In fact for the cloud case the error introduced by the scaling approximation is larger in the sort wave. This can be explained by the fact that the scaling factor b now increases with wave number and thus we expect the approximate and reference radiances to be in better agreement in the long wave region of the spectrum.

For the Stratus Maritime cloud type (Figures 37 and 38) the radiance attenuation is smaller than the one observed for the Straus Continental cloud since (see Figure 11) the scattering coefficients is smaller. The error introduced by the scaling approximation is still less than 1 K in the thermal infrared but it now significantly smaller in the short wave where it does not exceed 3 K. This can be partly explained by the fact that in the short wave the scaling factor b for the Stratus Maritime cloud is smaller than the one for the Stratus Continental type.

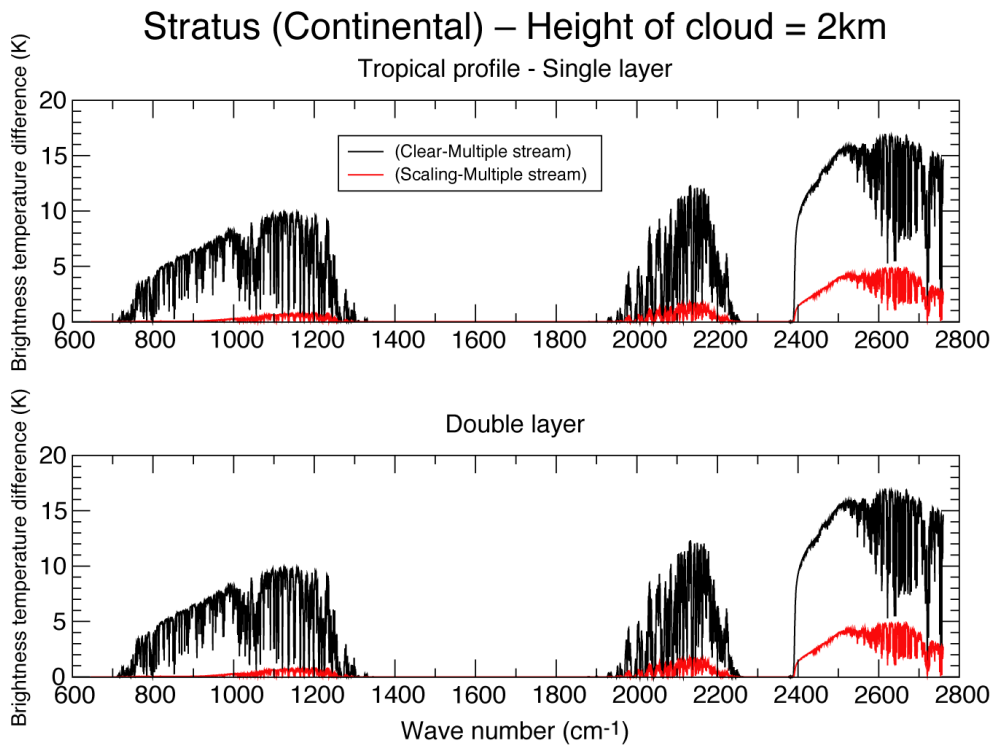


Figure 35 The radiative impact of the Stratus Continental cloud type (black curve) and the error introduced by the scaling approximation (red curve) for the tropical profile for two different values of the cloud thickness.

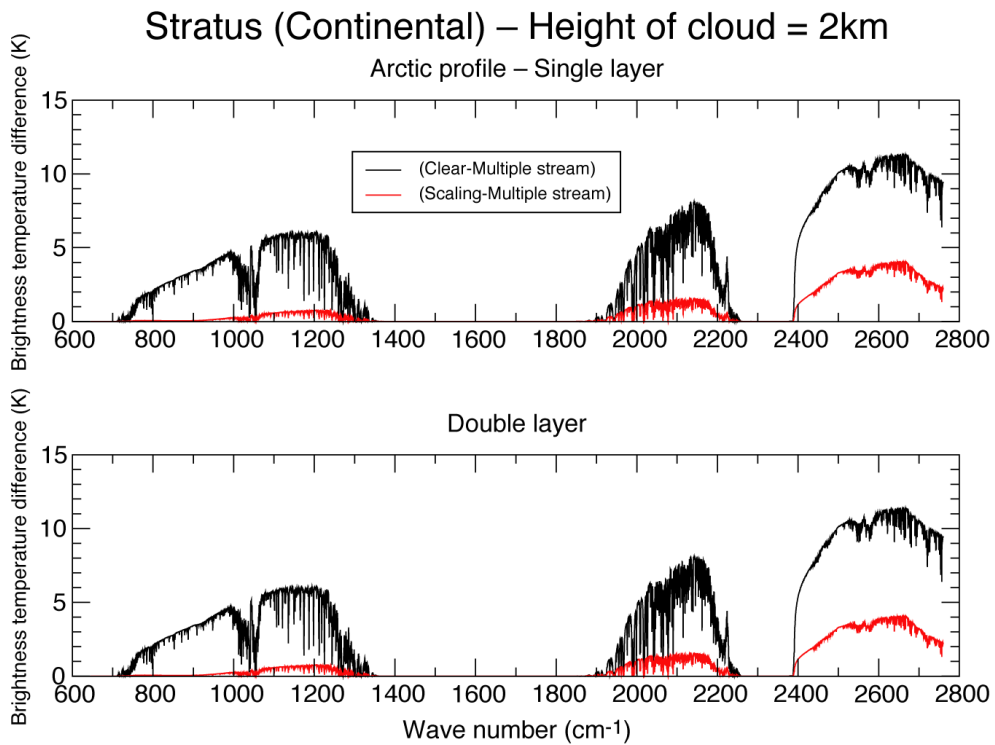


Figure 36 The radiative impact of the Stratus Continental cloud type (black curve) and the error introduced by the scaling approximation (red curve) for the arctic profile for two different values of the cloud thickness.

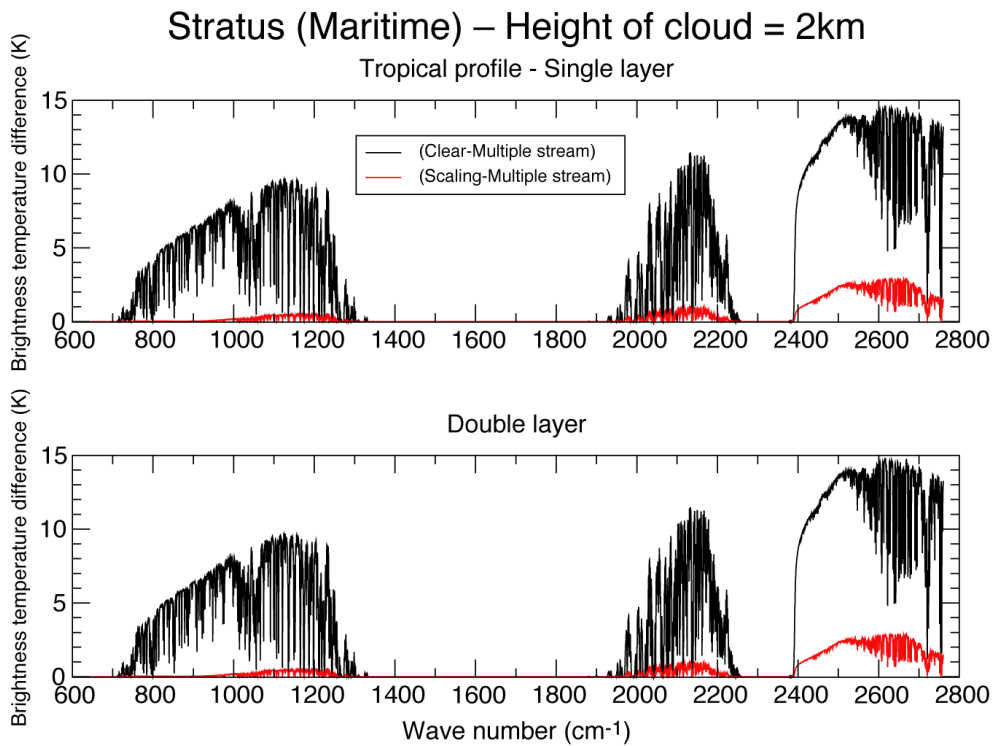


Figure 37 The radiative impact of the Stratus Maritime cloud type (black curve) and the error introduced by the scaling approximation (red curve) for the tropical profile for two different values of the cloud thickness.

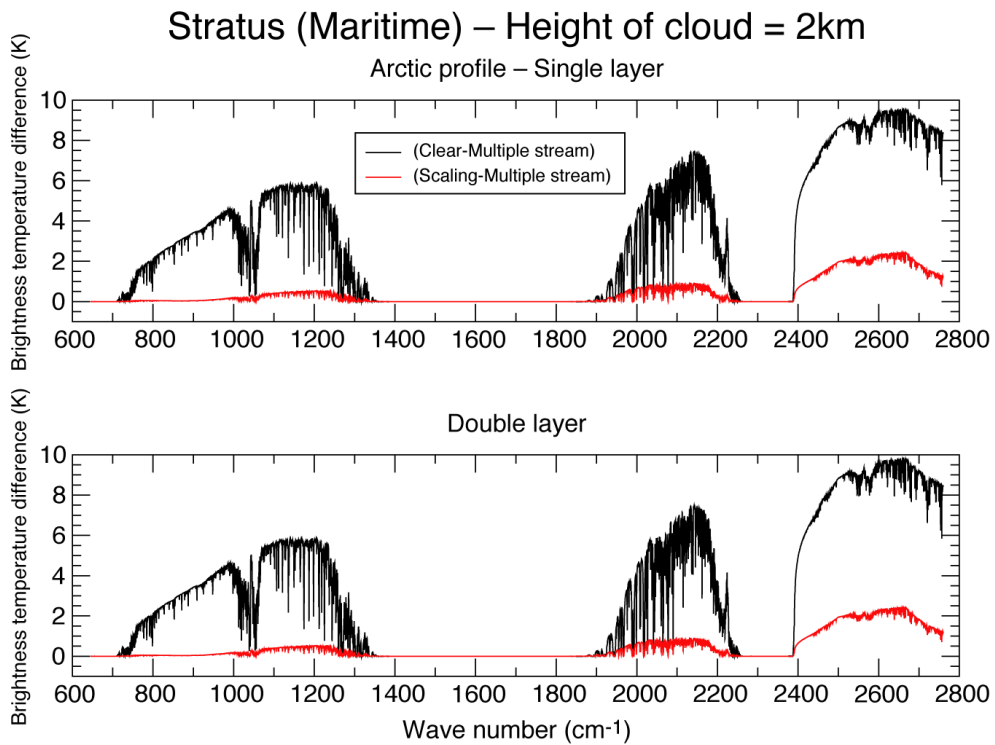


Figure 38 The radiative impact of the Stratus Maritime cloud type (black curve) and the error introduced by the scaling approximation (red curve) for the arctic profile for two different values of the cloud thickness.

Results for the middle level clouds are shown in Figures 39 to 44. Since the top of the cloud is placed at a higher altitude, we now expect the radiance attenuation to affect a larger portion of the spectrum since more channels will have the peak of the weighting functions at or below the cloud level. This can be readily assessed comparing Figures 35 and 39. For the low level cloud the radiance attenuation is not affecting the spectral region between 1350 cm^{-1} and 1950 cm^{-1} whereas for the middle level cloud the spectral range not affected by the radiance attenuation is narrower (from 1400 cm^{-1} to 1800 cm^{-1}). This effect is all the more evident for the arctic profile (compare Figures 36 and 40) since the peak of the weighting functions is situated at lower altitudes (i.e. more channels are influenced by the presence of a middle level cloud). In terms of radiance attenuation, similar results are observed for the Cumulus Continental Clean and the Cumulus Continental Polluted. The radiance attenuation can be as large as 40 K in the short wave and 30 K in the thermal infrared. The error introduced by the scaling approximation does not exceed 2 K in the thermal infrared and is less than 7 K in the short wave. For the Cumulus Maritime type a somewhat smaller radiance attenuation is observed above all in the shortwave. Note how the error introduced by the scaling approximation is significantly lower for this cloud type. It is smaller than 0.8 K in the thermal infrared and does not exceed 1.2 K in the short wave. In fact, among the middle level cloud types, the Cumulus Maritime cloud is characterized by a lower value of the scaling parameter b across the whole spectral range.

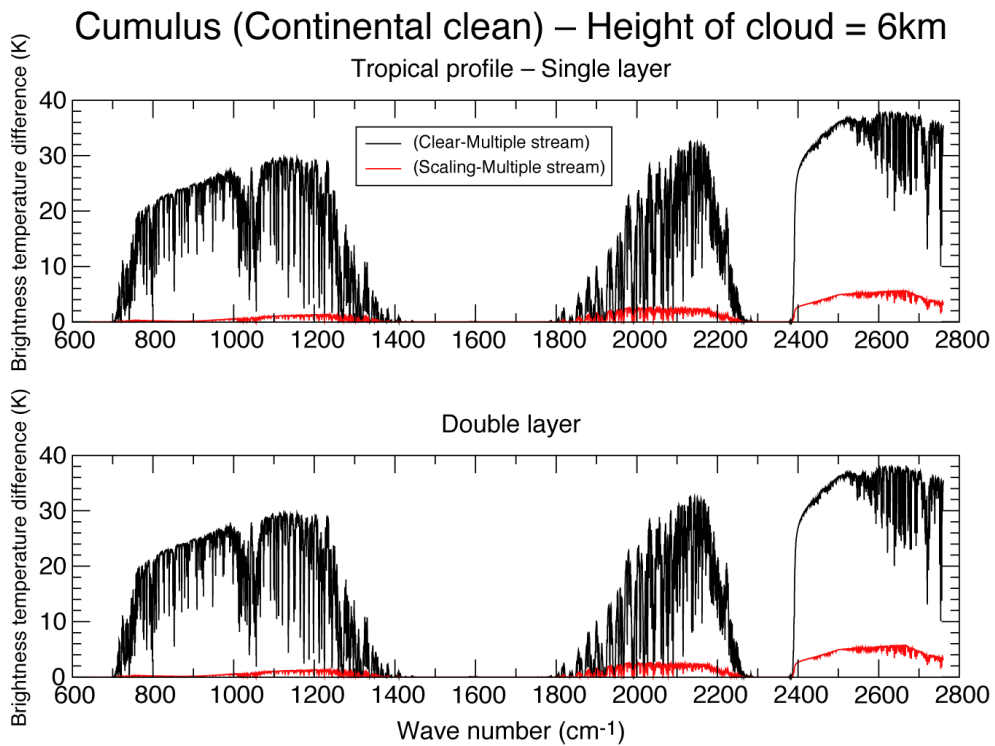


Figure 39 The radiative impact of the Cumulus Continental Clean cloud type (black curve) and the error introduced by the scaling approximation (red curve) for the tropical profile for two different values of the cloud thickness.

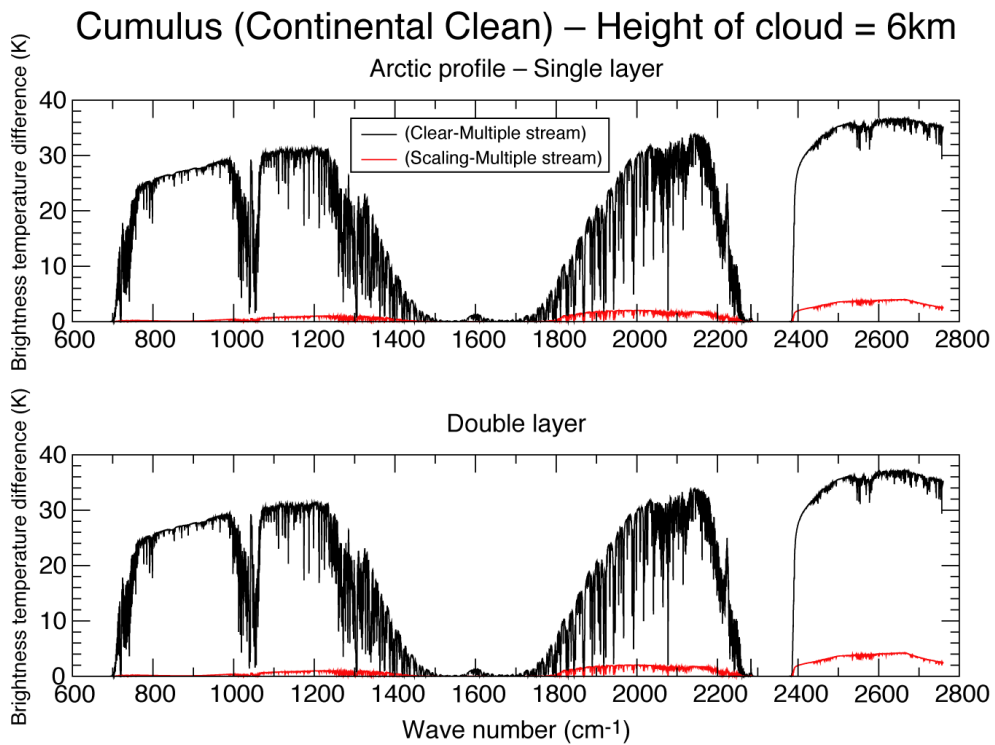


Figure 40 The radiative impact of the Cumulus Continental Clean cloud type (black curve) and the error introduced by the scaling approximation (red curve) for the arctic profile for two different values of the cloud thickness.

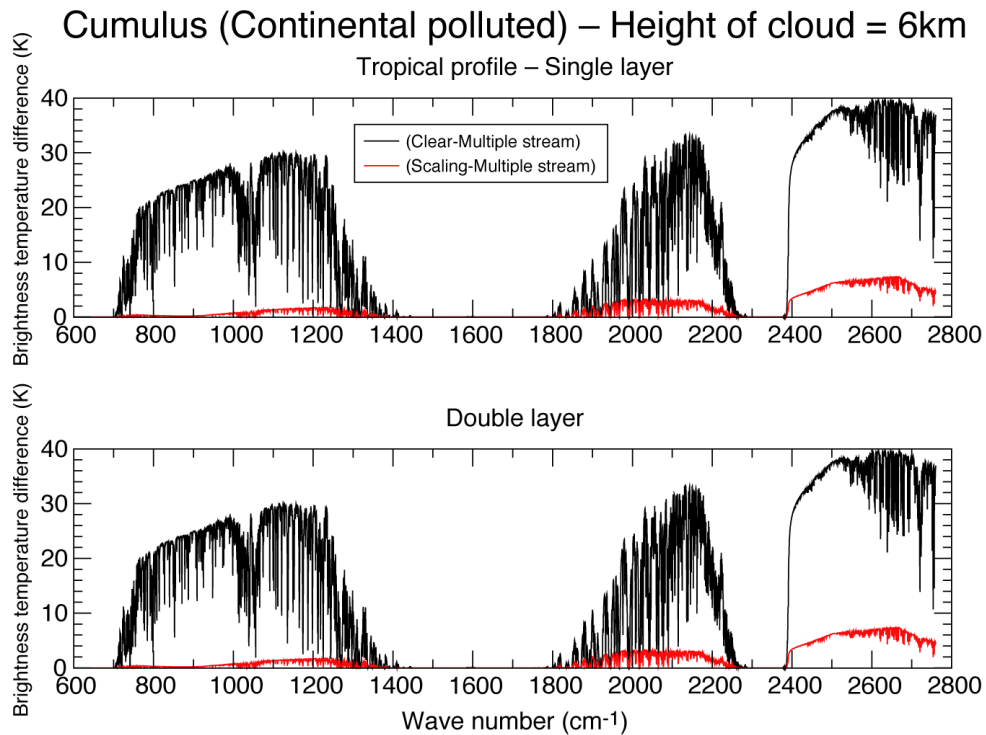


Figure 41 The radiative impact of the Cumulus Continental Polluted cloud type (black curve) and the error introduced by the scaling approximation (red curve) for the tropical profile for two different values of the cloud thickness.

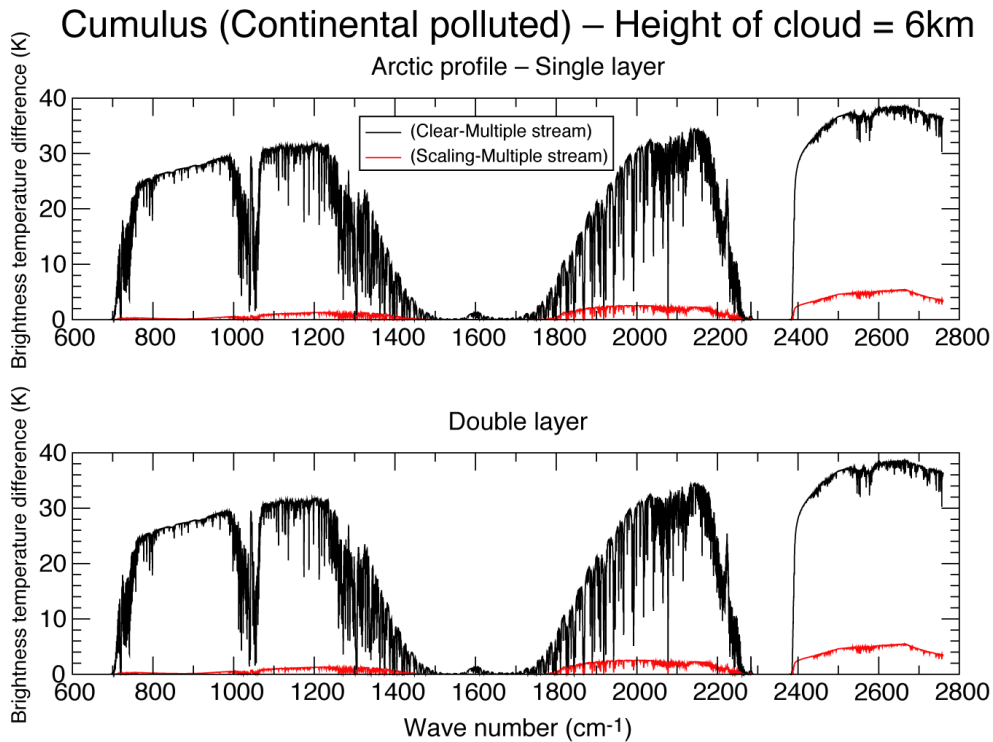


Figure 42 The radiative impact of the Cumulus Continental Polluted cloud type (black curve) and the error introduced by the scaling approximation (red curve) for the arctic profile for two different values of the cloud thickness.

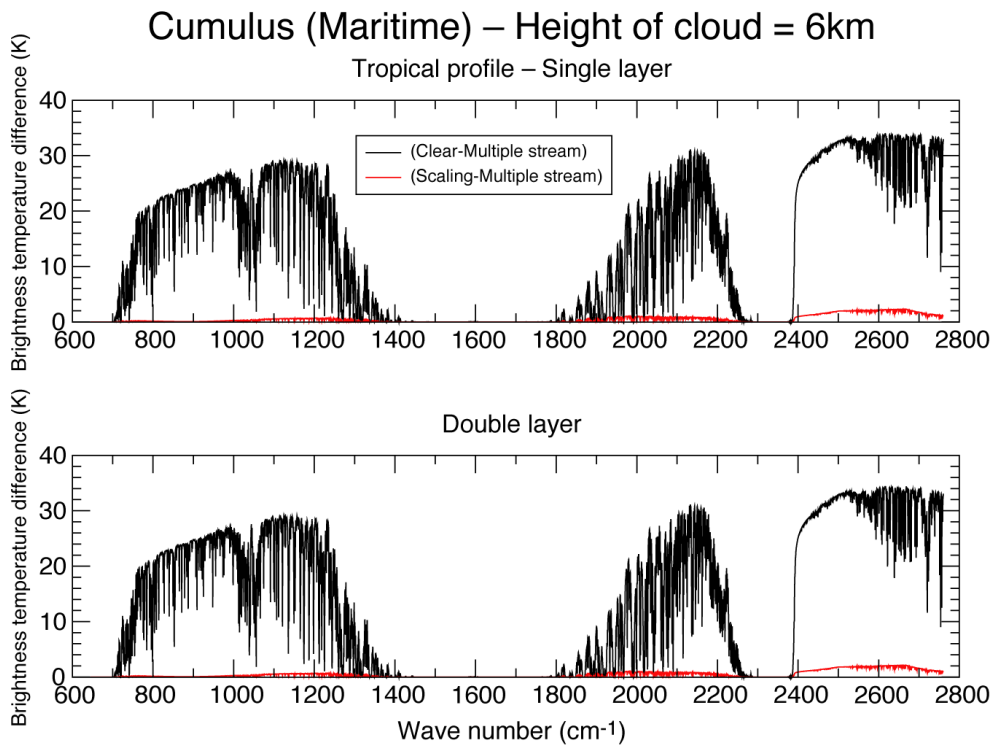


Figure 43 The radiative impact of the Cumulus Maritime cloud type (black curve) and the error introduced by the scaling approximation (red curve) for the tropical profile for two different values of the cloud thickness.

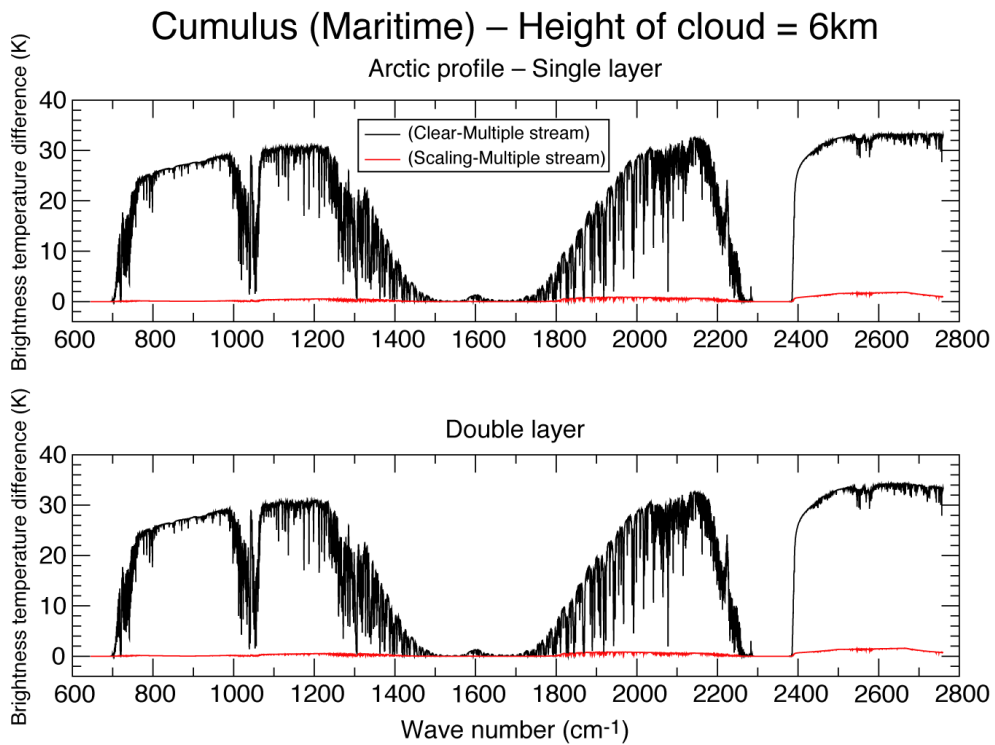


Figure 44 The radiative impact of the Cumulus Maritime cloud type (black curve) and the error introduced by the scaling approximation (red curve) for the tropical profile for two different values of the cloud thickness.

7.3 The results for cirrus clouds

The spectra for the cirrus cloud types have been computed by placing the top height of the cloud at 12 km, 10 km and 7 km. This equivalent to a cloud thickness of 400 m for the 12 km and 10 km cases and a cloud thickness of 300 m for the 7 km case. The effect of introducing an additional cloud of the same type in the adjacent lower atmospheric layer has also been investigated. Note how for the tropical profile a cirrus cloud could not be placed at 7 km since the average temperature of the layer is outside the range covered by the Heymsfeld and Platt size distribution. This is also partly true for the 10 km case where for the same reason we could not double the thickness of the cloud. The number densities representative of average conditions for the various temperature intervals are listed in Table 7 where the correspondent values of the ice water content can also be found. Results are plotted in Figures 45 to 49 where the top and bottom panels show results for the single layer cloud and double layer cloud respectively.

Results plotted in Figure 45 show that for the 12 km case the radiance attenuation is now affecting the whole spectral range with exception of the regions characterized by the presence of channels whose weighting functions peak well above the cloud. The radiance attenuation can reach 10 K in the thermal infrared and 5 K in the short wave. Note how, because of the moderate optical thickness of the cirrus cloud, doubling the thickness of the cloud results in a considerably larger attenuation.

A remarkable feature is the accuracy achieved by the scaling approximation. The error never exceeds 0.5 K. This can be justified by the nature of the phase function for the ice crystal that is characterized by a very narrow and sharp forward peak that results in very small value of the b parameter. This is shown in Figure 13 where it can be seen the asymmetry parameter is larger than 0.9 across the whole spectral range. Note how for the cirrus cloud case the scaling approximation tends to underestimate the radiance in contrast to what happens for the aerosols and water clouds where the scaling approximation always overestimate the radiance. Partly because the particle density decreases dramatically with lower temperatures (see Figure 12), the radiance attenuation for the arctic profile is sensibly lower than the attenuation for the tropical profile. For this case the error introduced by the scaling approximation is typically below 0.1 K. For the lower cloud height of 10 km we observe a reduction of the radiance departure; less than 5 K for the tropical profile and less than 0.3 K for the arctic profile. The scaling approximation now introduces an error that is typically less than 0.2 K.

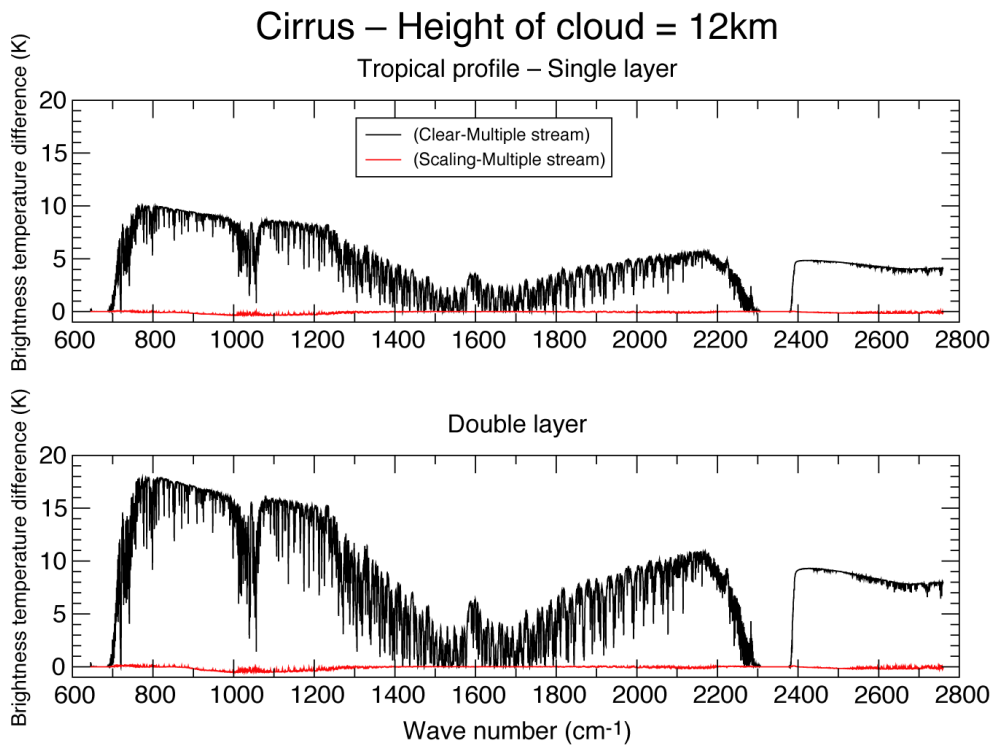


Figure 45 The radiative impact of the Cirrus cloud type (black curve) and the error introduced by the scaling approximation (red curve) for the tropical profile for two different values of the cloud thickness.

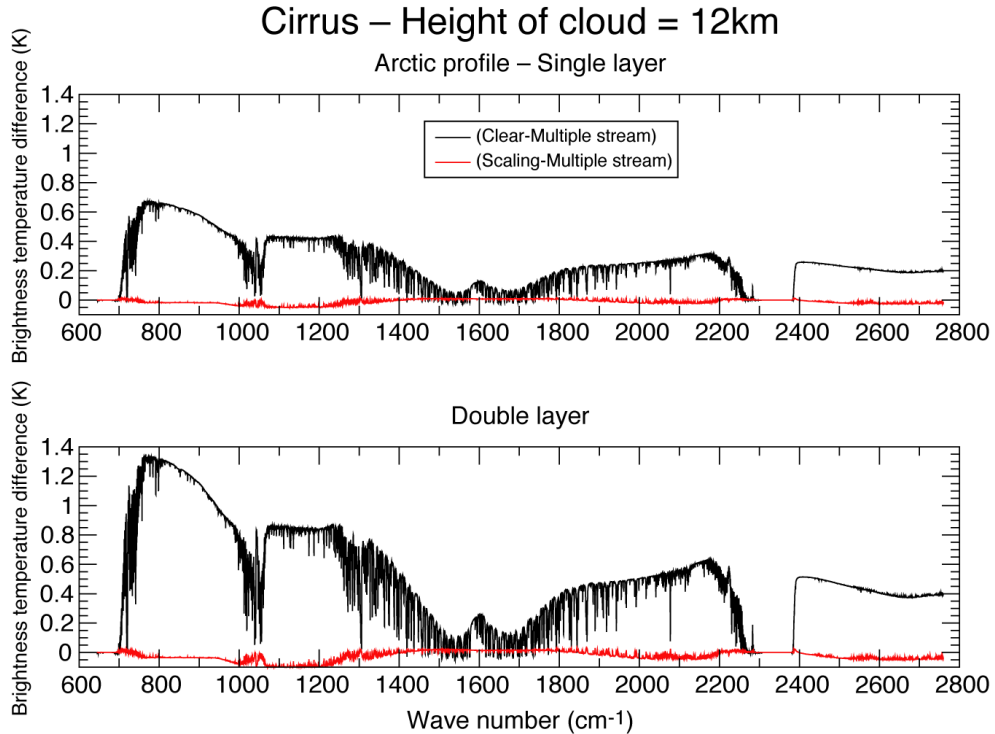


Figure 46 The radiative impact of the Cirrus cloud type (black curve) and the error introduced by the scaling approximation (red curve) for the arctic profile for two different values of the cloud thickness.

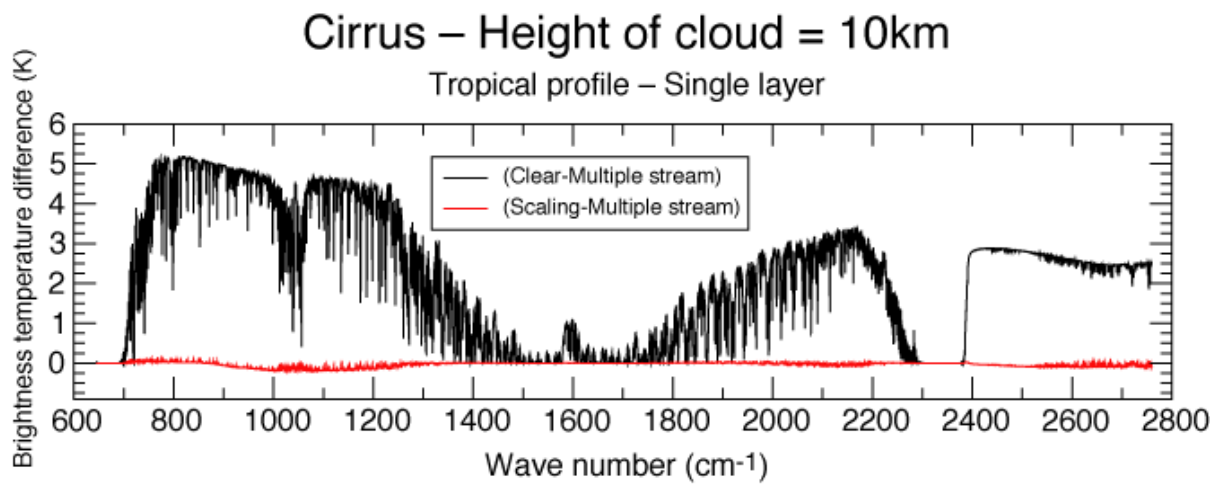


Figure 47 The radiative impact of the Cirrus cloud type (black curve) and the error introduced by the scaling approximation (red curve) for the tropical profile.

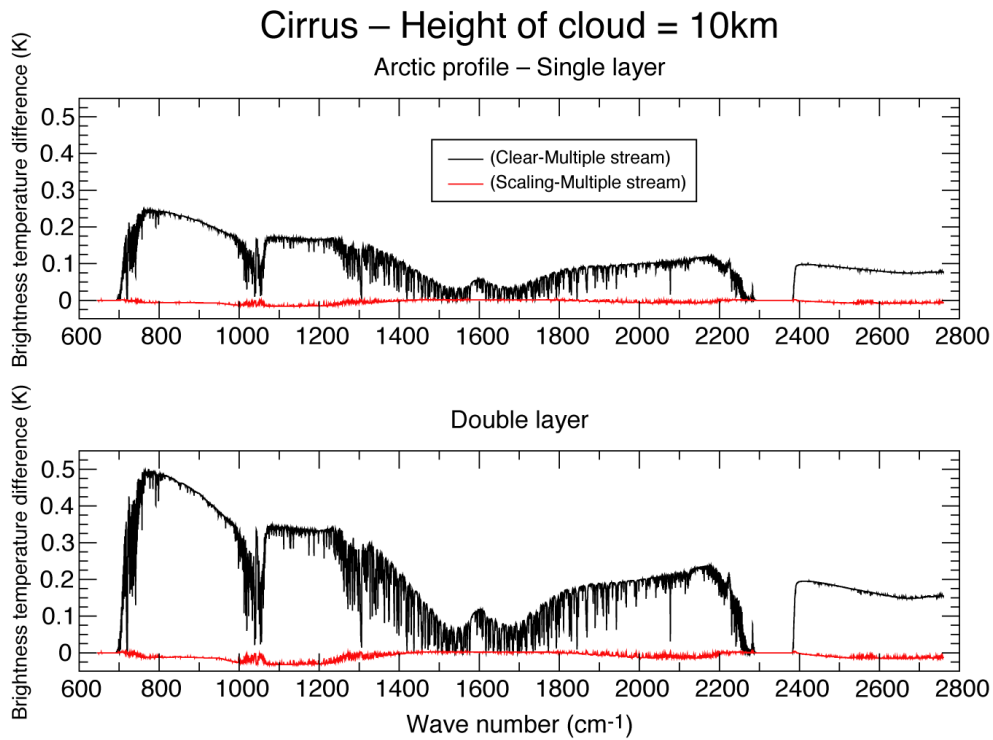


Figure 48 The radiative impact of the Cirrus cloud type (black curve) and the error introduced by the scaling approximation (red curve) for the tropical profile for two different values of the cloud thickness.

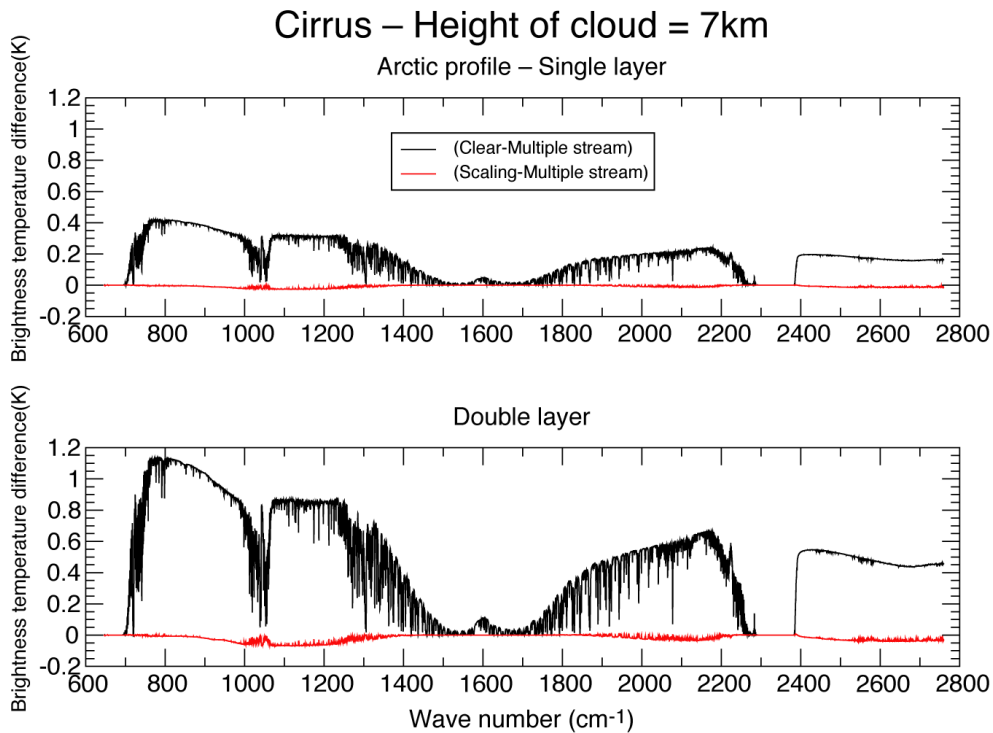


Figure 49 The radiative impact of the Cirrus cloud type (black curve) and the error introduced by the scaling approximation (red curve) for the tropical profile for two different values of the cloud thickness.

8. Conclusions

A new version of RTIASI, RTIASI-5, has been developed that features the radiative transfer in presence of aerosols and clouds. Multiple scattering is parameterized by scaling the optical depth by a factor derived by including the backward scattering in the emission of a layer and in the transmission between levels. This parameterisation of multiple scattering rests on the hypothesis that the diffuse radiance field is isotropic and can be approximated by the Planck function. The scaling approximation has the advantage that the form of the radiative transfer equation does not differ too much from the one used in clear sky conditions and thus the computational efficiency of the code is not significantly degraded.

RTIASI-5 includes eleven aerosol components and five water cloud types. The database of optical properties for aerosols and water droplets has been generated using the Lorentz-Mie theory adopting the dataset of microphysical properties assembled in the Optical Properties of Aerosols and Clouds (OPAC) software package. In every atmospheric layer the RTIASI-5 user can define any mixture of aerosol components and then obtain the optical properties for a given situation or compute the optical properties for 10 aerosol types representative of average conditions for what is considered to be the range of climatological important aerosols. RTIASI-5 can also include eight different types of cirrus clouds. Cirrus clouds are assumed to be composed of hexagonal ice crystals. For RTIASI-5 we have generated a composite database of optical properties for ice crystals that uses the geometric optics (GO) method for large crystals and the T-matrix method for small crystals.

To improve the accuracy of the radiance computation in presence of optically thick layers, RTIASI-5 features a new parameterisation of the Planck function based on the 'linear in τ ' assumption that the source function throughout the layer is linear with the optical depth of the layer. When compared to the parameterization used in the previous version of the code, the application of the new source function results in top of the atmosphere radiance differences up to 0.15 K in clear sky conditions and up to 2 K in cloudy conditions.

To address the problem of radiative transfer in presence of a number of multiple layers partly covered by clouds, we have implemented a novel scheme (the stream method) that divides the atmosphere into a number of homogeneous columns. Each column is assigned a fractional area coverage and is characterized by different radiative properties since it can contain a different number of either cloud-free layers or totally cloudy layers. Once the top of the atmosphere radiance is computed for each column, the total radiance is obtained as the sum of all the radiances weighted by the column area coverage.

To assess the accuracy of the scaling approximation we have compared approximate radiances with reference radiances computed by using a doubling-adding algorithm. Results have been obtained for each aerosol and cloud type for a tropical and arctic profile. The desert aerosol type has the largest impact on the radiance. The inclusion of desert dust in a tropical profile can result in a reduction of the top of the atmosphere radiance by 4K in the thermal infrared and by 1.8K in the short wave if an above average concentration is assumed. For this case, errors introduced by the scaling approximation are less than 1K in the thermal infrared and less than 0.25 K in the short wave. For the urban aerosol type the radiance attenuation can be as large as 1 K in the thermal infrared and 0.6 K in the short wave. For the other aerosol types a smaller radiance attenuation is observed; this seldom exceeds 0.1 K for the average concentration case and 0.5 K for the above the average concentration case. Errors introduced by the scaling approximation are typically small. For the Urban type these never exceeds 0.1 K whereas for the other aerosol types they are typically below 0.05 K. For all aerosol types, errors observed in the thermal infrared are larger than those observed in the short wave.

For the low level clouds (Stratus Continental and Stratus Maritime) the radiance attenuation resulting from the introduction of the cloud is larger in the shortwave and can reach 16 K for the tropical profile and 11 K for the arctic profile. The error introduced by the scaling approximation for the tropical profile is less than 1 K in the thermal infrared and can be as large as 5 K in the short wave for the Stratus Continental. For the Stratus Maritime cloud the error introduced by the scaling approximation is still less than 1 K in the thermal infrared and does not exceed 3 K in the short wave.

Results for the middle level clouds (Cumulus Continental Clean, Cumulus Continental Polluted and Cumulus Maritime) show that the radiance attenuation can be as large as 40 K in the short wave and 30 K in the thermal infrared. The error introduced by the scaling approximation does not exceed 2 K in the thermal infrared and is less than 7 K in the short wave for the Cumulus Continental Clean and Cumulus Continental Polluted. For the Cumulus Maritime type a smaller radiance attenuation is observed above all in the shortwave. The error introduced by the scaling approximation is significantly lower for this cloud type. It is smaller than 0.8 K in the thermal infrared and does not exceed 1.2 K in the short wave.

Finally, for the cirrus cloud type we found a remarkable agreement between approximate and reference radiances. For the tropical profile the error introduced by the scaling approximation never exceeds 0.5 K whereas for the arctic profile is typically below 0.1 K.

Acknowledgments

We are very grateful to M. Khanert, SMHI, for having provided the T-Matrix code and for many helpful discussions. We also wish to thank A. Macke, Leibnitz-Institut fuer Meereswissenschaften, for having provided the GO code. Discussions with M. Hess, DLR, P. Bauer, ECMWF, P. Watts, ECMWF, and R. Rizzi, Universita' di Bologna, were also very valuable during the course of this work.

References:

- Amorati, R., and Rizzi, R., 2002: Radiances simulated in presence of clouds by use of a fast radiative transfer model and a multiple-scattering scheme. *Applied Optics*, Vol **41**, No. 9, pp. 1604-1614.
- Bauer, P., 2002: Microwave radiative transfer modelling in clouds and precipitation. Part I: Model description. *ECMWF NWP SAF Programme Research Report*, NWPSAF-EC-TR-005 (available from: <http://www.ecmwf.int/publications/library/do/references/list/202>)
- Cayla, F., 1993: IASI infrared interferometer for operations and research. In “*High Spectral Resolution Infrared Remote Sensing for Earth's Weather and Climate Studies*”, NATO ASI Series 1, Ed. A. Chedin, M. Chaine and N. Scott.
- Chou, M.-D., Lee, K.-T., Tsay, S.-C., and Fu, Q., 1999: Parameterization for Cloud Longwave scattering for Use in Atmospheric Models. *Journal of Climate*, **12**, pp. 159-169.
- Draine, B., T., and Flatau, P., J., 1994: Discrete-dipole approximation for scattering calculations. *J. Opt. Soc. Am. A. Opt. Image Sci.*, **11**, pp. 1491-1499.
- Hess, M., Kepke, P., and Schult, I., 1998: Optical Properties of Aerosols and Clouds: the software package OPAC. *Bul. Am. Met. Soc.*, **79**, pp. 831-844.

- Kahnert, F.M., Stamnes, J., and Stamnes, K., 2001: Application of the extended boundary condition method to homogeneous particles with point-group symmetries. *Applied Optics*, Vol **40**, No.18, pp. 3110-3123.
- Klaes, K.,D., Buhler, Y., Wilson, H., and Wollenweber, F., 2000: The EUMETSAT Polar System: mission and products. *Proceedings of the 2000 EUMETSAT Meteorological Satellite Data User's Conference*, Bologna, Italy, 29 May-2 June 2000.
- Liou, K.N., 2002: An introduction to Atmospheric radiation. Academic Press, San Diego.
- Macke, A., Mueller, J., and Raschke, E., 1996: Single scattering properties of Atmospheric Ice Crystals. *Journal of the Atmospheric Sciences*, Vol. **53**, No.19, pp2813-2825.
- Matricardi, M., and Saunders, R., 1999: Fast radiative transfer model for simulation of infrared atmospheric sounding interferometer radiances. *Applied Optics*, **38**, pp 5679-5691.
- Matricardi, M., 2003: RTIASI-4, a new version of the ECMWF fast radiative transfer model for the infrared atmospheric sounding interferometer. *ECMWF Technical Memorandum 425*. (available from: <http://www.ecmwf.int/publications/library/do/references/list/14>)
- Mishchenko, M., Hovenier, J., W., and Travis, L., D., 2000: *Light scattering by Nonspherical Particles*. Academic Press, San Diego.
- Rabier, F., Thepaut, J.,N., and Courtier, P., 1998: Extended assimilation and forecast experiments with a four dimensional variational assimilation scheme. *Q. J. R. Meteorol. Soc.*, **124**, pp.1861-1887.
- Takano, Y., and Liou, K., N., 1989: Solar radiative transfer in cirrus clouds. I. Single scattering optical properties of hexagonal ice crystals. *J. Atmos. Sci.*, **46**, pp20-36.
- Trotsenko, A., Kurchatov Institute (personal communication, 2003).
- Van de Hulst, H.C., 1981: *Light Scattering by Small Particles*. Dover Publications, New York.
- Yang, P., and Liou, K., N., 1996: Finite-difference time domain method for light scattering by small ice crystals in three-dimensional space. *J. Opt. Soc. Am.*, **13**, pp 2072-2085.

APPENDIX A

The configuration of the input profile for aerosols

a) *The mixture of aerosol components is defined by the user*

The input profile is configured in the form of a matrix characterized by 11 columns and 89 rows. Each column represents each of the 11 aerosol components and each row represents each of the 89 layers the atmosphere is divided into. To include an aerosol component in the radiative transfer, the user has to assign the average value of the number density (in units of cm^{-3}) in the layer. If a zero number density is found, then the aerosol component will not be included in the radiative transfer. Each column should be assigned to each aerosol component as follows:

Column 1:	Insoluble	(INSO)
Column 2:	Water soluble	(WASO)
Column 3:	Soot	(SOOT)
Column 4:	Sea salt (acc. mode)	(SSAM)
Column 5:	Sea salt (coa. mode)	(SSCM)
Column 6:	Mineral (nuc. mode)	(MINM)
Column 7:	Mineral (acc. mode)	(MIAM)
Column 8:	Mineral (coa. mode)	(MICM)
Column 9:	Mineral transported	(MITR)
Column 10:	Sulphate droplets	(SUSO)
Column 11:	Volcanic ash	(VOLA)

In Figure 50 an example is given where a mixture of insoluble and water-soluble components is specified in some atmospheric layers.

	INSO	WASO	SOOT	SSAM	SSCM	MINM	MIAM	MICM	MITR	SUSO	VOLA
	0	0	0	0	0	0	0	0	0	0	0
	0	0	0	0	0	0	0	0	0	0	0
1350	0.9	0	0	0	0	0	0	0	0	0	0
1600	0.11	0	0	0	0	0	0	0	0	0	0
1800	0.12	0	0	0	0	0	0	0	0	0	0
2000	0.13	0	0	0	0	0	0	0	0	0	0
2400	0.14	0	0	0	0	0	0	0	0	0	0
0	0	0	0	0	0	0	0	0	0	0	0
0	0	0	0	0	0	0	0	0	0	0	0

Figure 50. An example of input profile for aerosol components

b) *The mixture of aerosol components is chosen among those proposed as default in RTIASI-5*

In this case an input file is supplied as default in RTIASI-5 that contains ten different profiles. In each profile a different combination of aerosol components is given that is representative of a climatological aerosol type (see Table 3 for details). Once the user has specified the aerosol type, the aerosol profile is then read from the input file and the number densities of each aerosol component can be optionally scaled by the same constant factor.

The configuration of the input profile for clouds

The input profile is configured in the form of a matrix characterized by 6 columns and 89 rows. Each column represents each of the 6 cloud types and each row represents each of the 89 layers the atmosphere is divided into. The first five columns are assigned to water clouds, the last column is assigned to cirrus clouds. Each column should be assigned to each cloud type as follows:

- Column 1: Stratus Continental (STCO)
- Column 2: Stratus Maritime (STMA)
- Column 3: Cumulus Continental Clean (CUCC)
- Column 4: Cumulus Continental Polluted (CUCP)
- Column 5: Cumulus Maritime (CUMA)
- Column 6: Cirrus (CIRR)

To include a water cloud type in the radiative transfer, the user has to assign the average value of the liquid water content (in units of $g\ m^{-3}$) in the layer. To include a cirrus cloud type in the radiative transfer, the user has to assign the average value of the ice water content (in units of $g\ m^{-3}$) in the layer. If a zero value is found, then the cloud will not be included in the radiative transfer. Note that two different cloud types are not allowed in the same layer. If this is the case, RTIASI-5 will return an error message and the execution of the code will be stopped.

In addition to the profile that contains information on the cloud water/ice content, a second profile has to be provided that contains information on the cloud fractional cover in the layer. The cloud fractional cover is a number ranging from 0 (cloud free) to 1 (totally overcast). Examples of input profiles for clouds are given in Figure 51 and Figure 52.

STCO	STMA	CUCC	CUCP	CUMA	CIRR
0	0	0	0	0	0.026
0	0	0	0	0	0
0	0	0	0	0	0
0.	0	0.26	0	0	0
0	0	0	0	0	0
0	0	0	0	0	0
0.28	0	0	0	0	0
0	0	0	0	0	0

Figure 51 An example of the cloud liquid/ice water content input profile for some atmospheric layers.

STCO	STMA	CUCC	CUCP	CUMA	CIRR
0	0	0	0	0	0.8
0	0	0	0	0	0
0	0	0	0	0	0
0	0	0.5	0	0	0
0	0	0	0	0	0
0	0	0	0	0	0
0.3	0	0	0	0	0
0	0	0	0	0	0

Figure 52 An example of the cloud fractional coverage input profile for some atmospheric layers.